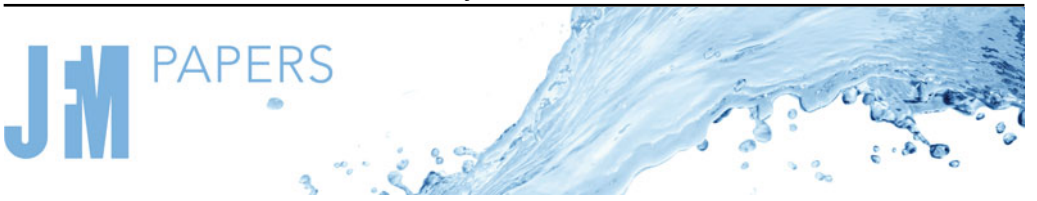
J. Fluid Mech. (2026), *vol.* 1041, A38, doi:10.1017/jfm.2026.11928



Addressing bedload flux variability due to grain-shape effects and experimental channel geometry

Thomas Pähtz[1], Yulan Chen[2], Jiafeng Xie[2,3], Remi Monthiller[4], Raphael Maurin[5], Katharina Tholen[6], Yen-Cheng Lin[7], Hao-Che Ho[7], Peng Hu[2], Zhiguo He[2] and Orencio Duran[8]

[1]School of Marine Science and Engineering, South China University of Technology, Guangzhou 511442, PR China

[2]Institute of Port, Coastal and Offshore Engineering, Ocean College, Zhejiang University, Zhoushan 316021, PR China

[3]State Key Laboratory of Fluid Power and Mechatronic Systems and Department of Engineering Mechanics, Zhejiang University, Hangzhou 310027, PR China

[4]Aix-Marseille University, CNRS, Centrale Marseille, Institut de Recherche sur les Phénomènes Hors Équilibre (IRPHÉ), Marseille 13384, France

[5]Université de Toulouse, Toulouse INP, CNRS, IMFT, Toulouse 31400, France

[6]Institute for Theoretical Physics, Leipzig University, Postfach 100920, Leipzig 04009, Germany

[7]Department of Civil Engineering, National Taiwan University, Taipei City 106, PR China

[8]Department of Ocean Engineering, Texas A&M University, College Station, TX 77843-3136, USA

Corresponding authors: Thomas Pähtz, tpaehtz@gmail.com; Peng Hu, pengphu@zju.edu.cn; Zhiguo He, hezhiguo@zju.edu.cn

(Received 15 November 2025 UTC; revised 10 July 2026 UTC; accepted 15 July 2026 UTC)

The study-to-study variability of bedload flux measurements in turbulent sediment transport borders an order of magnitude, even for idealised laboratory conditions. This uncertainty stems from physically poorly supported, empirical methods to account for channel geometry effects in the determination of the transport-driving bed shear stress, and from study-to-study grain-shape variations. Here, we derive a universal method of bed shear stress determination. It consists of a granular-physics-based definition of the bed surface and a channel sidewall correction based on linking Reynolds stress to bulk flow properties via Kolmogorov's theory of turbulence. Application of this method to bedload transport of spherical grains – to rule out grain-shape effects – collapses data from existing laboratory measurements and grain-resolved computational fluid dynamics (CFD) and discrete element method (DEM) simulations for various channel geometries onto a single curve. In contrast, classical sidewall corrections, as well as an alternative bed surface definition, are unable to universally capture these data, especially those from shallow

© The Author(s), 2026. Published by Cambridge University Press.

https://doi.org/10.1017/jfm.2026.11928 Published online by Cambridge University Press

or very narrow channel flows. We then apply our method to an extended grain-shape-controlled data compilation, complemented by literature data for non-spherical grains and from grain-unresolved CFD-DEM simulations. This compilation covers a very diverse range of transport conditions, ranging from very narrow to infinitely wide channels, from shallow to deep channel flows, from mild to steep bed slopes, and from weak to intense transport. We generalise an existing physical bedload flux model to account for grain-shape effects, and show that it explains almost all the compiled data within a factor of only 1.3.

Key words: sediment transport, multiphase and particle-laden flows, channel flow

1. Introduction

Bedload transport is a special kind of sediment transport in which typically coarse sedimentary grains roll, slide and hop along the surface in response to the shearing of a loose granular bed by a flow of liquid. It plays a vital role in shaping the environments of Earth and other planetary bodies (Poggiali *et al.* 2016) by promoting the formation and growth of geological features of various scales, including ripples and dunes (Charru *et al.* 2013; Durán Vinent *et al.* 2019), deltas and fans (Baker *et al.* 2015), and laminations and cross-bedding (Schieber 2016; Shchepetkina *et al.* 2019). A key problem hampering our understanding of bedload-induced landscape evolution is the notoriously large noise commonly associated with measurements of the bedload flux, often exceeding an order of magnitude (Recking 2010; Ancey & Recking 2023). It partially originates from huge non-Gaussian flux fluctuations over large time scales, which even occur under steady flow conditions in the laboratory due to continuous topographic change (Dhont & Ancey 2018). However, also when restricted to steady flows over flat beds at short time scales, reported bedload fluxes can still substantially differ between laboratory studies for largely self-similar conditions, for both weak and intense transport-driving flows (Ancey & Recking 2023), and it has been unclear whether such differences arise due to physical or experimental reasons. On the one hand, physical reasons may come into play because dissimilarities in grain size and shape distributions are not accounted for by commonly used similarity parameters. On the other hand, study-to-study variability of the geometry of laboratory facilities is a potential culprit on the experimental side, especially in view of the associated large random and systematic uncertainties in the experimental determination of the transport-driving bed shear stress τ_b (Yager *et al.* 2018). Focusing here on rectangular open channels, since they are geometrically similar to natural streams, the ratio b/h between the channel width b and flow depth h is a crucial parameter in this regard. Ideally, one would want b/h to be as large as possible to most closely resemble bedload transport in nature. However, in experimental reality, b/h is often of order unity, substantially weakening the shearing of the bed due to frictional losses at the sidewalls, causing the flow to be non-uniform in the cross-channel direction (Guo 2015). Another important parameter is the ratio between h and the grain diameter d. For shallow channel flows where h/d is close to unity, the method by which the bed surface elevation, and thus the flow depth h above it, is identified can have a large effect on the value of τ_b.

To illustrate that channel geometry effects often are not appropriately accounted for, we choose two laboratory studies measuring bedload flux over a flat bed: Ni & Capart (2018), who conducted their experiments in a wide but shallow channel ($h/d \sim 2{-}6$), and Deal *et al.* (2023), who used a very narrow but deep channel ($b/h \approx 0.1$). Since the grains in both studies were spherical and relatively uniformly sized, one expects the same quantitative behaviour of the non-dimensionalised bedload flux Q_* as a function of

https://doi.org/10.1017/jfm.2026.11928 Published online by Cambridge University Press

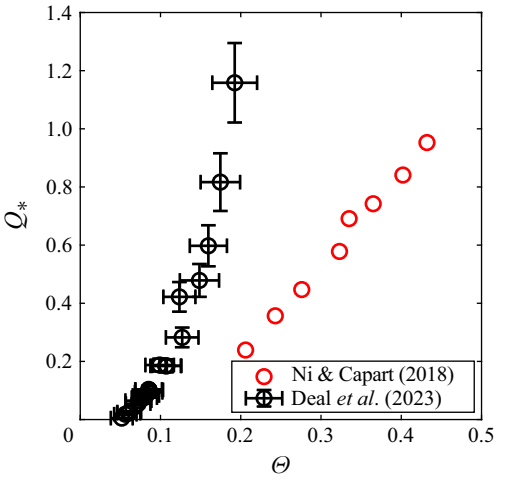


Figure 1. Bedload flux measurements for spherical grains by Ni & Capart (2018) and Deal *et al.* (2023). The Shields number Θ and non-dimensionalised bedload flux Q_* are defined and determined as described in these studies. For $\Theta \approx 0.2$, the values of Q_* disagree with each other by a factor of approximately 6.

the non-dimensionalised bed shear stress or Shields number Θ (Ancey 2020). However, when using these studies' reported values for Θ and Q_*, based on their own definitions and methods to determine τ_b, both datasets disagree with each other by a staggering factor of approximately 6 for $\Theta \approx 0.2$ (figure 1). This indicates that at least one of them was inappropriately correcting for channel geometry effects, showcasing the need for a universal channel geometry correction method.

This study addresses two of the mentioned potential reasons for the study-to-study variability of laboratory bedload flux measurements: grain shape and channel geometry effects. We compile existing and new data of turbulent bedload transport along flat beds (no bedforms) of shape-controlled and (relatively) uniformly sized grains, obtained from experiments and grain-resolved (i.e. directly resolving fluid–particle interactions) and grain-unresolved numerical simulations based on various computational fluid dynamics/discrete element method (CFD-DEM) techniques, across channel flow widths and heights, grain shapes, bed slopes and flow strengths. In § 2, we reconcile channel geometry effects in these data through a universal sidewall correction, based on linking Reynolds stress to bulk flow properties via an extension of Kolmogorov's theory of turbulence (Gioia & Bombardelli 2002; Gioia & Chakraborty 2006), and a granular-physics-based definition to precisely determine the bed surface elevation (Pähtz & Durán 2018*b*). This channel geometry correction method is validated, among others, through a collapse of experimental and grain-resolved numerical bedload flux data for spherical grains on a unique behaviour, whereas classical methods (Einstein 1942; Johnson 1942; Guo 2015, 2017) yield very large scatter. Furthermore, in § 3, we generalise an existing physical bedload flux model (Pähtz & Durán 2020) to account for grain-shape effects. It agrees with the entire channel-geometry-corrected data compilation within a factor 1.3. The results are then discussed in § 4, and conclusions are drawn in § 5.

2. Universal channel geometry correction method

In this section, we derive and validate a universal channel geometry correction method to determine the transport-driving bed shear stress τ_b for open channels with hydraulically

https://doi.org/10.1017/jfm.2026.11928 Published online by Cambridge University Press

rough sediment beds and hydraulically smooth sidewalls. We begin with the definition of τ_b (§ 2.1), and derive from it, partially using known results, an expression that contains the flow depth h and the effective mixture sidewall shear stress τ_w as unknowns. We then propose to determine h from an existing granular-physics-based definition of the bed surface elevation (§ 2.2), and derive an expression for τ_w/τ_b from an extension of Kolmogorov's theory of turbulence (§ 2.3). In § 2.4, the resulting channel geometry correction method is tested against a data compilation of turbulent bedload transport of spherical grains and other data.

2.1. *Definition of bed shear stress*

For turbulent bedload transport in open channels with hydraulically rough sediment beds, there is a limited region in the clear-water flow above the bedload layer where the streamwise (x) fluid velocity profile $u_x(z)$ approximately obeys the logarithmic law of the wall (Kidanemariam 2016; Jain *et al.* 2021; Deal *et al.* 2023):

$$u_x \approx \frac{u_\tau}{\kappa} \ln \frac{z+z_o}{z_o}, \tag{2.1}$$

where $\kappa = 0.41$ is the von Kármán constant, z is the bed-normal coordinate, with $z=0$ the bed surface elevation, z_o is the hydrodynamic roughness, which depends on both grain size and bedload flux (Durán *et al.* 2012), and u_τ is the friction velocity. The latter defines the bed shear stress $\tau_b \equiv \rho_f u_\tau^2$, where ρ_f is the fluid density. In what follows, we seek to express τ_b in terms of known fluid and channel parameters.

Kidanemariam (2016) and Jain *et al.* (2021) conducted direct numerical simulations (DNS) with the DEM of bedload transport driven by negative streamwise fluid pressure gradients χ at zero bed slope angle α for infinitely wide and relatively deep channel flows. Both studies found that τ_b defined via (2.1) is equivalent to the effective mixture shear stress evaluated at the bed surface $\sigma_{zx}(0)$. Below, we generalise this result to open channels with sidewalls and arbitrary α.

For a statistically steady ($\partial_t = 0$) and streamwise uniform ($\partial_x = 0$) open-channel flow, the mixture momentum balance resulting from averaging over time t and the streamwise direction x reads (Pähtz *et al.* 2026)

$$\partial_y \tilde{\rho}\tilde{u}_y\tilde{u}_x + \partial_z \tilde{\rho}\tilde{u}_z\tilde{u}_x = \partial_y \tilde{\sigma}_{yx} + \partial_z \tilde{\sigma}_{zx} + \chi + \tilde{\rho} g \sin\alpha, \tag{2.2}$$

where g is the gravitational acceleration, $\tilde{\rho}$ is the mixture density, $\tilde{\boldsymbol{u}}$ is the mixture velocity, and $\tilde{\boldsymbol{\sigma}}$ is the mixture shear stress tensor, which is composed of the averaged viscous fluid shear stress, the solid phase contact stress, a stress resulting from fluid–particle interactions, and the mixture Reynolds stress. Integrating (2.2) over height and the cross-channel coordinate y, written using the notations $\langle\cdot\rangle_z \equiv (1/h)\int_0^h \cdot\, \mathrm{d}z$ and $\langle\cdot\rangle_y \equiv (1/b)\int_{-b/2}^{b/2} \cdot\, \mathrm{d}y$, then yields

$$-b\left[\langle\tilde{\sigma}_{zx} - \tilde{\rho}\tilde{u}_z\tilde{u}_x\rangle_y\right]_{z=0}^{z=h} = h\left[\langle\tilde{\sigma}_{yx} - \tilde{\rho}\tilde{u}_y\tilde{u}_x\rangle_z\right]_{y=-b/2}^{y=b/2} + bh\chi + bh\langle\langle\tilde{\rho}\rangle_y\rangle_z\, g\sin\alpha. \tag{2.3}$$

When assuming impermeable boundary conditions at the bed ($\langle\tilde{\rho}\tilde{u}_z\rangle_y(0) = 0$) and free surface ($\langle\tilde{\rho}\tilde{u}_z\rangle_y(h) = 0$) on average, statistical steadiness and mass conservation would imply impermeable boundary conditions also at the sidewalls ($\langle\tilde{\rho}\tilde{u}_y\rangle_z(\pm b/2) = 0$) on average, and vice versa. Although these boundaries are not necessarily perfectly impermeable, since low vertical transport may occur through the bed surface, we assume impermeability for simplicity, in which case the terms $-\langle\tilde{\rho}\tilde{u}_z\tilde{u}_x\rangle_y(0,h)$ and $-\langle\tilde{\rho}\tilde{u}_y\tilde{u}_x\rangle_z(\pm b/2)$ are Reynolds-like fluctuation stresses. We therefore identify $\sigma_{zx} \equiv \langle\tilde{\sigma}_{zx} - \tilde{\rho}\tilde{u}_z\tilde{u}_x\rangle_y$, when evaluated at $z=0$ or $z=h$, as the effective mixture bed

https://doi.org/10.1017/jfm.2026.11928 Published online by Cambridge University Press

and free-surface shear stresses, respectively, and $\tau_w \equiv \mp(\langle\tilde{\sigma}_{yx} - \tilde{\rho}\tilde{u}_y\tilde{u}_x\rangle_z)(\pm b/2)$ as the effective mixture sidewall shear stress. Furthermore, we use the free-surface boundary condition $\sigma_{zx}(h) = 0$ and the relation $\langle\tilde{\rho}\rangle_y = (1-\phi)\rho_f + \phi\rho_p$ (Pähtz *et al.* 2026), where ρ_p is the particle density, and $\phi(z)$ is the cross-channel-averaged particle volume fraction, and define the sediment transport load $M \equiv \rho_p h\langle\phi\rangle_z$ (the average mass of transported grains – i.e. grains elevated above the bed surface – per unit area of the bed surface) and the vertical submerged gravitational acceleration $\tilde{g}_z \equiv (1-\rho_f/\rho_p)g\cos\alpha$. Inserting these relations and definitions, and dividing by b, (2.3) becomes

$$\sigma_{zx}(0) = h(\chi + \rho_f g\sin\alpha) - (2h/b)\tau_w + M\tilde{g}_z\tan\alpha. \tag{2.4}$$

This expression is a generalisation of the mixture balance by Bagnold (1956) to the case of a channel with sidewalls ($h/b > 0$), and of the clear-water balance by Guo (2015) to the case of a mixture ($M > 0$); Guo (2015) also assumed $\chi = 0$. Since we later propose a Bagnoldian-type bedload transport model, we assume, analogous to Bagnold (1956), that the bed shear stress defined via (2.1) is given by

$$\tau_b = \sigma_{zx}(0) - M\tilde{g}_z\tan\alpha. \tag{2.5}$$

This assumption is the generalisation of the mentioned finding $\tau_b = \sigma_{zx}(0)$ for $\alpha = 0$ (Kidanemariam 2016; Jain *et al.* 2021). Note that the alternative assumption that $\tau_b = \sigma_{zx}(0)$ for all α would lead to substantial disagreement between the bedload transport model presented in § 3.1 and the numerical data against which it is tested. Combining (2.4) and (2.5) yields

$$\tau_b = h(\chi + \rho_f g\sin\alpha) - (2h/b)\tau_w. \tag{2.6}$$

Here, τ_b depends on two unknowns: the bed surface elevation $z = 0$ required to determine h, and the effective mixture sidewall shear stress τ_w. They are addressed below.

2.2. *Definition of bed surface elevation*

The water depth h is the average distance between the free surface ($z = h$) and bed surface ($z = 0$) elevations. Many studies on bedload transport have treated h like it is a well-defined entity, without elaborating on what exactly they mean when referring to the bed surface (e.g. Deal *et al.* 2023). This non-specificity is acceptable in situations where, regardless of the precise definition of the bed surface elevation $z = 0$, the resulting h is much larger than the grain size d (e.g. Deal *et al.* 2023). This is because distinct definitions of $z = 0$ usually differ from one another only by a fraction of d, and therefore yield only small uncertainty in the value of h for such deep channel flows due to $h \gg d$. However, for shallow channel flows, the situation is fundamentally different, and a definition that accounts for the relevant grain scale characteristics and/or processes is required.

Most studies have defined $z = 0$ via assuming that the relevant grain scale characteristics are the random close packing and near-stationarity of the granular bed underneath $z = 0$. For example, $z = 0$ has been defined as the elevation where ϕ is a constant proportion of the bed packing fraction (Durán *et al.* 2012; Rebai *et al.* 2022), via a yield criterion (Maurin *et al.* 2015), via critical values of the average particle velocity v_x (Rebai *et al.* 2022) or associated shear rate $\dot{\gamma} = \mathrm{d}_z v_x$ (Capart & Fraccarollo 2011), or a nearly diminishing bedload flux below $z = 0$ (Ni & Capart 2018). However, since we later propose a Bagnoldian-type bedload transport model, we are more interested in a definition that accounts for the key assumptions behind such models.

Pähtz & Durán (2018*b*) demonstrated that there are essentially three assumptions integral to Bagnoldian-type bedload transport models: (i) the vast majority of transport occurs above $z > 0$; (ii) the ratio $\mu_b \equiv -\sigma^p_{zx}(0)/\sigma^p_{zz}(0)$ between the bed surface particle

https://doi.org/10.1017/jfm.2026.11928 Published online by Cambridge University Press

shear stress $\sigma_{zx}^{p}(0)$ and surface particle pressure $-\sigma_{zz}^{p}(0)$ is approximately constant; and (iii) except for intense transport conditions, the bed surface fluid shear stress $\sigma_{zx}^{f}(0)$ reduces to approximately the threshold shear stress τ_t. They argued that these assumptions are also expected to be satisfied for the flow-driven saltation of grains along a rigid, rough wall instead of a granular bed, and therefore looked for a criterion that characterises grain rebounds at a rough wall. From drawing an analogy to inclined granular flow, they hypothesised that close to the wall, $-\sigma_{zz}^{p}\dot{\gamma}$, which describes the rate at which the granular flow converts mean particle kinetic energy density into solid phase Reynolds stress $-\rho_p\phi v_z v_x$, should peak. Translating this hypothesis to sediment transport scenarios, they therefore defined the bed surface elevation through

$$\max(\dot{\gamma}\,\Sigma\phi) = (\dot{\gamma}\,\Sigma\phi)(0), \tag{2.7}$$

with $\Sigma\,\phi(z) \equiv \int_z^h \phi(z')\,\mathrm{d}z'$, based on the approximation $\sigma_{zz}^{p} \approx -\rho_p\,\Sigma\phi\tilde{g}_z$. They found that in their coupled Reynolds-averaged Navier–Stokes (RANS) DEM simulations of bedload transport (and windblown sand), when $z=0$ is defined through (2.7), it indeed approximately satisfies the three above assumptions across their simulated transport conditions.

2.3. *Sidewall correction*

Equation (2.6) is the same as that for clear-water flow (Guo 2015), except for generalised meanings of τ_b and τ_w. In particular, the bed shear stress τ_b, even though it is based on the mixture flow above the bed surface, controls, like its clear-water counterpart, the slope of the logarithmic velocity profile in (2.1) (Kidanemariam 2016; Jain *et al.* 2021; Deal *et al.* 2023). Like previous studies on the sidewall correction for open-channel flows with sediment transport (Einstein 1942; Johnson 1942; Vanoni & Brooks 1957; Guo 2015), we therefore model τ_b and τ_w as if the the flow above the bed surface were clear-water flow.

We start by rearranging (2.6) into the form

$$\tau_b = \frac{h(\chi + \rho_f g \sin\alpha)}{1 + (2h/b)\,f_w/f_b}, \tag{2.8}$$

where $f_w \equiv \tau_w/(\rho_f U^2)$ and $f_b \equiv \tau_b/(\rho_f U^2)$ are the friction factors associated with the sidewalls and bed surface, respectively, with U the bulk fluid flow velocity. The rougher these surfaces are, the larger is the rate at which the bulk flow energy density $\rho_f U^2/2$ is frictionally dissipated, and the larger is the shear stress applied at them. The difficulty is now to relate the friction factor ratio f_w/f_b to bulk flow properties, such as the open-channel flow geometry and U. In fact, one wants to avoid linking f_w/f_b to local flow properties, such the near-bed and near-sidewall flow velocity gradients, since they are usually not readily accessible.

A classical approach employed in numerous studies is to assume $f_w = f_b$, in which case $\tau_b = \tau_R \equiv R(\langle\chi\rangle_z + \rho_f g \sin\alpha)$, with $R \equiv hb/(b+2h)$ the hydraulic radius of the open channel (Guo 2015). This prediction is consistent with measurements of centreline flow velocity profiles in particle-free open channels consisting of only hydraulically smooth walls (sidewalls and bottom wall) for a large range of width-to-depth ratios ($b/h = 1.04{-}9.5$) (Yang *et al.* 2005). However, in bedload transport, where the bed surface is typically hydraulically rougher than the hydraulically smooth sidewalls ($f_b > f_w$), τ_R merely constitutes a lower bound of τ_b.

Another classical approach is the one by Einstein and Johnson (Einstein 1942; Johnson 1942; Vanoni & Brooks 1957; Guo 2017) (see Appendix A), in which f_w is determined from the empirical von Kármán–Prandtl law as the friction factor of a hydraulically fully

https://doi.org/10.1017/jfm.2026.11928 Published online by Cambridge University Press

smooth channel, then f_b is linked to f_w via an *ad hoc* separation of the open channel into three parallel, non-interacting sidewall-free channels. However, this separation's only physical justification is its mathematically constructed consistency at the extreme limit $f_b = f_w$, where it rightfully predicts $\tau_b = \tau_R$.

Our approach presented below does not rely on Einstein's *ad hoc* channel separation, but instead employs, for the Reynolds shear stress τ_s at a given surface (the sidewalls or the bed surface), a relation based on Kolmogorov's theory of turbulence (Gioia & Bombardelli 2002; Gioia & Chakraborty 2006):

$$\tau_s = -\rho_f \langle u'_\parallel u'_\perp \rangle = \kappa_\tau \rho_f U u_s, \tag{2.9}$$

where $\langle\cdot\rangle$ denotes an averaging procedure, and κ_τ is a flow-geometry-dependent empirical coefficient. Equation (2.9) states that the surface-parallel velocity fluctuations $u'_\parallel$ are dominated by the largest turbulent eddies in the system, whose characteristic velocity is U, whereas the surface-normal velocity fluctuations $u'_\perp$ are primarily controlled by the largest normal velocities u_s that turbulent eddies can generate near the surface. This relation, which was previously used to physically derive Manning's (Gioia & Bombardelli 2002) and Nikuradse's (Gioia & Chakraborty 2006) empirical formulas, leads to $f_w/f_b = u_w/u_b$, where u_b and u_w are the values of u_s for the hydraulically rough bed surface and hydraulically smooth sidewalls, respectively.

One may question (2.9), since it assumes that the sizes of the eddies associated with the bed and those associated with the sidewalls are independent of each other. Einstein's sidewall correction exhibits an analogous characteristic, and Guo (2015) therefore challenged it by noting that it would produce a uniform shear stress on all boundaries, $\tau_b = \tau_w = \tau_R$, in hydraulically fully smooth or hydraulically fully rough channels, which should not be the case due to secondary flows. However, we reiterate that for hydraulically fully smooth channels, $\tau_b = \tau_R$ is well supported by measurements of centreline velocity profiles for a large range of width-to-depth ratios ($b/h = 1.04$–9.5) (Yang *et al.* 2005), and we therefore believe that the assumption of independent eddy sizes is justified, at least in the context of determining τ_b.

The sizes of the eddies governing u_b and u_w are controlled by the typical size r of the protrusion of bed surface grains (which roughly corresponds to the size of the largest eddies that fit into the cavities of the bed surface) and the thickness $5(\kappa_\epsilon \kappa_u^3/2)^{-1/4} R\, Re^{-3/4}$ of the viscous sublayer adjacent to the hydraulically smooth sidewalls (Gioia & Chakraborty 2006), respectively, where $Re \equiv UR/\nu$ is the bulk flow Reynolds number, with ν the kinematic fluid viscosity. Furthermore, $\kappa_\epsilon = 5/4$ is a constant that follows from Kolmogorov's four-fifths law, and $\kappa_u \equiv u_R/U$ is a parameter that relates the characteristic velocity u_R of the largest eddies to U. It is found to be largely insensitive to flow geometry, with $\kappa_u = 0.036 \pm 0.005$ measured in pipe flow (Antonia & Pearson 2000), and $\kappa_u = 0.033$ in the atmospheric boundary layer (Tennekes & Lumley 1972). With these parameters, $f_w/f_b = u_w/u_b$ can be calculated via the smooth (f_w) and rough (f_b) limits of equation (2) of Gioia & Chakraborty (2006) as

$$\frac{f_w}{f_b} = 2^{1/12} \frac{\sqrt{\Gamma_{-2/3}(\beta/5)}\left[\beta(\kappa_\epsilon \kappa_u^3)^{-1/4}\right]^{1/3} Re^{-1/4}}{\sqrt{3/2}\,(r/R)^{1/3}} = c_{wb} \frac{Re^{-1/4}}{(r/R)^{1/3}}, \tag{2.10}$$

where $\Gamma_{-2/3}$ is the gamma function of order $-2/3$, $\beta = [3\Gamma(4/3)]^{3/4}$ is the characteristic constant of the exponential decay of the velocity spectrum of turbulent flow, with Γ the gamma function, and $c_{wb} \approx 2.23$ is the scaling coefficient resulting from evaluating the expression in the middle of (2.10). Note that the prefactor $2^{1/12}$ originates from the fact that R in Gioia & Chakraborty (2006) refers to the pipe radius, which is twice the hydraulic

https://doi.org/10.1017/jfm.2026.11928 Published online by Cambridge University Press

radius R here. Since c_{wb} depends only on κ_ϵ, κ_u and β, but not on the parameter κ_τ defined through (2.9), c_{wb} is an approximately channel-geometry-independent parameter.

Equation (2.10) states that f_w/f_b is the ratio between the Blasius friction factor $f_w \sim Re^{-1/4}$ for hydraulically fully smooth channels and the friction factor $f_b \sim (r/R)^{1/3}$ for hydraulically fully rough channels. Both scalings are of similar importance for the overall behaviour of f_w/f_b, and are readily accessible for typical sediment transport datasets (e.g. see table 1 for the values of Re and R/r for the channels with sidewalls considered in this paper). They require knowledge of the bulk fluid flow velocity U and bed grain protrusion size r, respectively. We calculate U from the fluid discharge Q_f as (Rebai *et al.* 2022)

$$U = \frac{Q_f}{b\left(h - \int_0^h \phi \, \mathrm{d}z\right)}. \tag{2.11}$$

Note that except for intense bedload transport, the term $\int_0^h \phi \, \mathrm{d}z$ has only a marginal effect on U. Hence for the datasets by Deal *et al.* (2023), which will constitute a part of our data compilation and for which concentration profile data are not available, we calculate U as $U \approx Q_f/(bh)$.

Furthermore, for random loose packed beds, like those in the classical experiments by Nikuradse (1933), where many bed surface grains protrude nearly fully into the flow, r is approximately equal to the size k of the physical roughness elements (Gioia & Bombardelli 2002; Gioia & Chakraborty 2006), and may be approximated as the volume-equivalent sphere diameter $d_o \equiv \sqrt[3]{6V_p/\pi}$, where V_p is the grain volume. However, in the context of bedload transport over mobile beds, the action of the flow smoothes out and compactifies the bed surface (Allen & Kudrolli 2018; Cúñez *et al.* 2022), since flow-mobilised bed surface grains tend to resettle in more resistant bed pockets (Clark *et al.* 2017). As a result, the longer a bed is exposed to flow, the less grains tend to protrude into it, and this process continues until a state of maximum resistance is reached (Pähtz *et al.* 2020). We estimate r in this state from laminar bedload experiments with spherical grains (Charru *et al.* 2004; Ouriemi *et al.* 2007; Houssais *et al.* 2015; Cúñez *et al.* 2022). They suggest that a Shields number $\Theta \approx 0.1$ is needed to mobilise grains in the state of maximal resistance, which we use to infer the typical pivoting angle of grains resting in bed pockets as $\psi \approx 60°$ from figure 13 of Agudo *et al.* (2017). It corresponds to a protrusion of $r = d\cos\psi \approx d/2$.

Moreover, for non-spherical grains, we exploit that grains transported at elevations close to the bed surface tend to align their largest projected area parallel to the bed due to torque (Jain *et al.* 2020; Zhang *et al.* 2025). We therefore choose the shortest grain axis c_g as the parameter setting r. It complements the large (a_g) and intermediate (b_g) grain axes, defined through approximating grains as ellipsoids. Hence we obtain $r = c_g/2$ as an estimate for sediment transport applications. However, when comparing to data obtained from open-channel flow over manually prepared fixed beds (Song 1994; Song & Chiew 2001) or artificial surfaces (Auel *et al.* 2014), we use the standard $r = d_o$ or $r = k$, respectively.

2.4. *Validation of the channel geometry correction method*

2.4.1. *Data compilation for turbulent bedload transport of spherical grains*

In order to isolate channel geometry effects on bedload flux, we compile existing experimental datasets for spherical grains, assuming that grain-shape effects are negligible for them. However, surprisingly, even though turbulent bedload transport has been studied for more than a century (Ancey 2020), flux measurements for spherical grains with a nearly uniform size distribution seem to be exceedingly scarce. (By contrast, such kinds of

https://doi.org/10.1017/jfm.2026.11928 Published online by Cambridge University Press

measurements are the rule rather than exception when studying bedload transport driven by laminar flow; e.g. Ouriemi *et al.* 2007; Aussillous *et al.* 2013; Houssais *et al.* 2015; Cúñez *et al.* 2022.) After an extensive literature search, we have managed to find only a handful of datasets (Frey *et al.* 2006; Frey 2014; Ni & Capart 2018; Armanini & Cavedon 2019; Carrillo *et al.* 2022; Deal *et al.* 2023). Four of these were subsequently disregarded because of either partially crystallised beds and very large scatter (Frey *et al.* 2006; Frey 2014), or the presence of substantial suspended load in addition to bedload (Armanini & Cavedon 2019), or self-inconsistent data (Carrillo *et al.* 2022) (almost no bedload flux change with important variation of flow strength: increasing bed slope at constant flow depth). The only two remaining experimental datasets for spherical grains are those by Ni & Capart (2018) and Deal *et al.* (2023) discussed in the Introduction. We therefore supplement the data compilation with additional datasets from numerical simulations that couple the DEM for the particle phase with a CFD method for the fluid phase that resolves the sub-grain scale: two datasets based on DNS (Kidanemariam & Uhlmann 2017; Jain *et al.* 2021) for infinitely wide channels ($b/h = \infty$, i.e. periodic boundaries), and two datasets based on grain-resolved large-eddy simulations (LES) (Zhang *et al.* 2022): one for $b/h = \infty$, and one for a narrow-deep-channel configuration ($b/h \approx 0.1$). Only such high-end methods, because they do not coarse-grain the particle phase and do not rely on empiricism for fluid-particle interactions, can be considered as similarly reliable as controlled experiments. The above spherical-grain datasets are denoted as D23EXPs, NC18EXP, Z22LESn, Z22LESw, J21DNS and KU17DNS, and summarised in table 1 together with other datasets used later. Note that to Z22LESn and Z25LESn (used later), we are unable to apply our sidewall correction method, since the bulk flow velocity U, or data from which it can be inferred, was not reported. In addition, wall-modelled LES such as these are known to underestimate the friction factors of channels with smooth walls (Nikitin *et al.* 2000; Yang *et al.* 2017), rendering (2.10) unusable. We therefore use the empirical sidewall correction that Zhang *et al.* (2025) applied to Z22LESn and Z25LESn, $\tau_b = 3\tau_R$, corresponding to $f_w/f_b \approx 0.29$, which is justified because it leads to an overlap with the sidewall-free simulations Z22LESw and Z25LESw, respectively, for otherwise almost the same conditions (table 1).

For the spherical-grain datasets discussed in the previous paragraph, we determine the bed surface elevation using the method described in § 2.2, provided that the required data are available from the studies. This is the case for the dataset NC18EXP (figure 2), but not for D23EXPs, Z22LESn, Z22LESw, J21DNS and KU17DNS. For the latter, we use the values reported in the respective studies. This approximation is justified for D23EXPs, Z22LESn, J21DNS and KU17DNS, since $h^* = h/d \gg 1$ (table 1). In the case of Z22LESw, the authors of the respective study (Zhang *et al.* 2022) stated that they employed the method by Pähtz & Durán (2018*a*) to calculate the bed surface elevation, which is the same as our method described in § 2.2. For more details and the calculation of the bed shear stress uncertainty, see Appendix B.

2.4.2. *Test of channel geometry correction methods against data compilation*

In this subsubsection, we test our existing channel geometry correction methods against the spherical-grain data compilation discussed above. Once the bed shear stress τ_b is determined using a given channel geometry correction method, we are able to fully characterise the hydrodynamic bedload transport conditions by dimensionless similarity parameters. We choose the particle–fluid density ratio $s \equiv \rho_p/\rho_f$, Galileo number $Ga \equiv d\sqrt{s\tilde{g}_z d}/\nu$, Shields number $\Theta \equiv \tau_b/(\rho_p \tilde{g}_z d)$, dimensionless flow depth $h^* \equiv h/d$, and bed slope angle α (table 1). All spherical-grain datasets (and also those for non-spherical grains

https://doi.org/10.1017/jfm.2026.11928 Published online by Cambridge University Press

https://doi.org/10.1017/jfm.2026.11928 Published online by Cambridge University Press

Experimental or numerical study	Width/depth ratio, b/h	Friction factor ratio, f_w/f_b	Grain shape	Shape parameters S_f	C_D	μ_s	Re	s	Hydrodynamic conditions Ga	Θ	α	h^*	R/r
D23EXPs (Deal *et al.* 2023)	0.09−0.16	0.31−0.36	Spheres	1	0.43	0.46	3760−6557	2.57	1334−1339	0.056−0.22	0.03−0.13	13−24	2.0
D23EXPe (Deal *et al.* 2023)	0.10−0.14	0.32−0.35	Ellipsoids	0.83	0.60	0.60	4340−5553	2.42	1312−1314	0.071−0.16	0.03−0.09	15−22	2.0
D23EXPc (Deal *et al.* 2023)	0.10−0.13	0.36−0.39	Chips	0.51	0.39	0.65	4258−5634	2.36	767−768	0.092−0.21	0.04−0.08	22−29	2.8
D23EXPg (Deal *et al.* 2023)	0.10−0.15	0.36−0.40	Gravel	0.68	0.54	0.78	4135−6344	2.48	733−735	0.086−0.26	0.04−0.11	20−32	2.9−3.0
D23EXPp (Deal *et al.* 2023)	0.09−0.12	0.38−0.41	Prisms	0.88	0.79	0.86	3769−4917	2.40	725	0.071−0.14	0.03−0.06	26−35	2.9−3.0
NC18EXP (Ni & Capart 2018)	5.2−7.5	0.39−0.42	Spheres	1	0.49	0.45	4427−8568	1.39	998	0.12−0.21	0.02−0.03	2.3−3.3	3.6−4.8
R22EXPc (Rebai *et al.* 2022)	2.8−4.5	0.36−0.75	Cylinders	0.84	0.32	0.60	3282−39287	1.42	738	0.25−1.06	0.05−0.06	8.7−14	12−16
R22EXPl (Rebai *et al.* 2022)	5.0−6.0	0.57−0.74	Lenses	0.55	0.45	0.62	6110−16151	1.37	196	0.99−1.65	0.03−0.05	15−18	23−26
Z22LESn (Zhang *et al.* 2022)	0.13	0.29*	Spheres	1	0.48	0.45	N/A	2.55	1354−1356	0.11−0.20	0.06−0.11	16−17	2.0
Z25LESn (Zhang *et al.* 2025)	0.12	0.29*	Gravel	0.67	0.64	0.75	N/A	2.47	615−617	0.12−0.36	0.03−0.10	29	3.3
Z22LESw (Zhang *et al.* 2022)	∞	N/A	Spheres	1	0.48	0.45	N/A	2.55	1378	0.047−0.14	0.01−0.03	4.6−22	9.1−43
Z25LESw (Zhang *et al.* 2025)	∞	N/A	Gravel	0.67	0.64	0.75	N/A	2.47	617	0.18−0.29	0.01−0.014	29−30	59−60
J21DNS (Jain *et al.* 2021)	∞	N/A	Spheres	1	N/A	N/A	N/A	2.55	44.7	0.13	0 ($\chi > 0$)	18	36
KU17DNS	∞	N/A	Spheres	1	N/A	N/A	N/A	2.5	28.37	0.096−0.19	0 ($\chi > 0$)	13	26
M18RANS (Maurin *et al.* 2018)	∞	N/A	Spheres	1	0.42	0.40	N/A	1.75−4	1259−2521	0.11−1.38	0.01−0.19	2.0−62	4.0−123
M19RANSs (Monthiller 2019)	∞	N/A	Spheres	1	0.42	0.49	N/A	2.5	1782	0.16−0.72	0.05	4.1−18	8.3−37
M19RANSt1 (Monthiller 2019)	∞	N/A	Triplets	0.85	0.42	0.55	N/A	2.5	1782	0.24−1.01	0.05	6.1−26	12−51
M19RANSt2 (Monthiller 2019)	∞	N/A	Triplets	0.75	0.42	0.63	N/A	2.5	1782	0.31−1.28	0.05	8.0−33	16−65
M19RANSt3 (Monthiller 2019)	∞	N/A	Triplets	0.71	0.42	0.68	N/A	2.5	1782	0.39−1.57	0.05	9.9−40	20−80
M19RANSt4 (Monthiller 2019)	∞	N/A	Triplets	0.62	0.42	0.72	N/A	2.5	1782	0.47−1.86	0.05	12−47	24−95
M19RANSt5 (Monthiller 2019)	∞	N/A	Triplets	0.58	0.42	0.69	N/A	2.5	1782	0.56−2.18	0.05	14−55	28−111
LES	∞	N/A	Spheres	1	0.54	0.49	N/A	2.56	1341	0.14−0.32	0 ($\chi > 0$)	18−22	35−44
LESCD	∞	N/A	Spheres	1	1.78	0.49	N/A	2.56	1341	0.17−0.26	0 ($\chi > 0$)	20−23	40−47
BLRANS1	∞	N/A	Spheres	1	2.24	0.38	N/A	[1.1, 2.65]	50	0.044−1.21	0−0.16	∞	∞
BLRANS2	∞	N/A	Spheres	1	1.46	0.38	N/A	[1.1, 2.65]	100	0.058−1.21	0	∞	∞
BLRANSCD	∞	N/A	Spheres	1	15.9	0.38	N/A	2.65	50	0.063−0.45	0	∞	∞

Table 1. Summary of bedload flux data shown in this study. The top, middle and bottom entries correspond to experiments, grain-resolved CFD-DEM simulations, and grain-unresolved CFD-DEM simulations, respectively. The data of the datasets BLRANS1 and BLRANS2 with $s = 2.65$ and $\alpha = 0$ are from Pähtz & Durán (2020). The datasets Z25LESn and Z25LESw do not include data from simulations based on the 'artificial- shrinkage method' by Zhang *et al.* (2025), since this method has been falsified (Chen *et al.* 2026). The asterisk $*$ indicates that the friction factor ratio f_w/f_b was not calculated but determined empirically. Note that the listed parameter values of C_D, Ga, Θ and h^* are based on $d = c_g$.

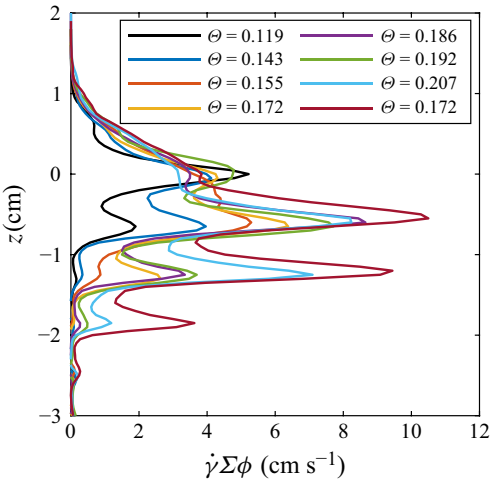


Figure 2. Determination of bed surface elevation for experimental dataset NC18EXP (Ni & Capart 2018). The vertical profiles of $\dot{\gamma}\,\Sigma\phi$ exhibit several local maxima due to layering. We choose the top-most local maximum as the bed surface elevation, since the vertical profile of the fluid shear stress $\sigma^f_{zx}(z)$ exhibits a focal point there, $\sigma^f_{zx}(0) \approx \tau_t$ (§ 2.4.3), consistent with the theoretical expectation (Pähtz & Durán 2018*b*).

considered later) are well within the range of what is typically categorised as bedload transport ($s \lesssim 10$; Pähtz & Durán 2020), and most of them also satisfy $s^{1/2}Ga \gtrsim 70$, here termed 'rough' transport conditions. In rough turbulent bedload, particle inertia dominates viscous fluid–particle interactions, and the non-dimensionalised bedload flux $Q_* \equiv Q/(\rho_p d\sqrt{s\tilde{g}_z d})$ is therefore expected to become essentially independent of s and Ga for sufficiently small α (Ancey 2020; Pähtz & Durán 2020; Zhang *et al.* 2022). We use this expectation as a tool to evaluate the different sidewall corrections outlined above (figure 3). It can be seen that the data for rough turbulent bedload transport of spherical grains indeed collapse, within measurement uncertainty, on a universal $Q_*(\Theta)$ behaviour for our method (figure 3*d*), but do not collapse at all when employing a classical method or left uncorrected (figures 3*a–c*), or when using our sidewall correction but a different bed surface definition (NC18EXP∗ in figure 3*d*). Note that the spherical-grain dataset Z22LESn is not included in figure 3(*c*), since the data for the bulk flow velocity U, required to calculate the Einstein–Johnson sidewall correction, are unavailable. Furthermore, Z22LESn in figure 3(*d*) is based not on our sidewall correction (since it also requires U as an input), but on the correction that Zhang *et al.* (2025) applied to this dataset, $\tau_b = 3\tau_R$.

2.4.3. *Further independent tests of our channel geometry correction method*

Figures 4(*a*) and 4(*b*) present further independent support for our sidewall correction. First, our correction predicts almost the same Shields numbers as those that Deal *et al.* (2023) empirically determined as $\tau_b = 2.41\tau_R$ via fitting (2.1) to their flow velocity data, for both spherical and non-spherical grains (figure 4*a*). Second, it is also consistent with experimental data from particle-free flows in open channels ($b/h = 2.94-7.79$) consisting of hydraulically rough beds and hydraulically smooth sidewalls (Song 1994; Song & Chiew 2001; Auel *et al.* 2014) (figure 4*b*).

Furthermore, the strong quantitative difference between the spherical-grain data by Ni & Capart (2018) and Deal *et al.* (2023) discussed in the Introduction (figure 1) is found to be

https://doi.org/10.1017/jfm.2026.11928 Published online by Cambridge University Press

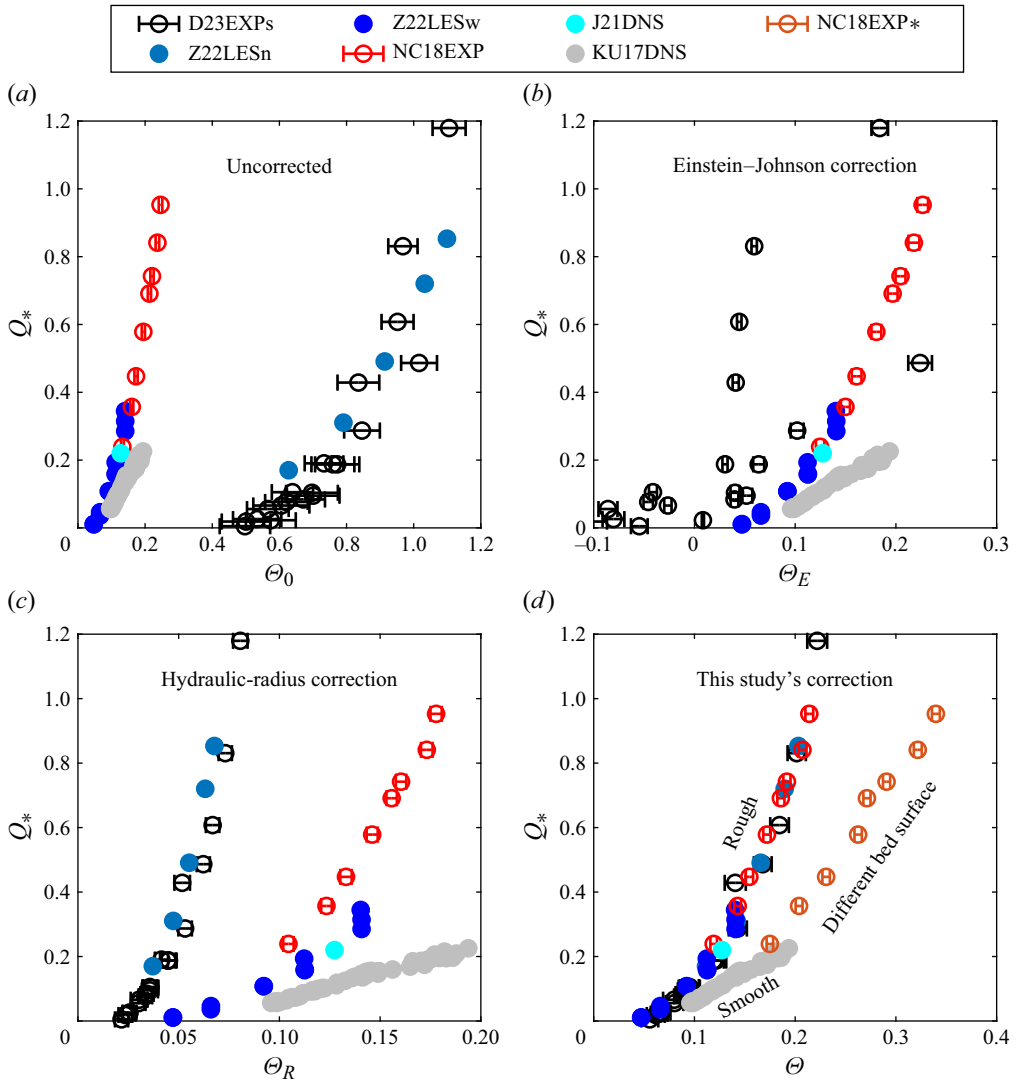


Figure 3. Channel geometry corrections. Non-dimensionalised bedload flux Q_* versus Shields numbers for spherical grains: (*a*) uncorrected for sidewall effects (Θ_0); (*b*) hydraulic-radius correction (Guo 2015) (Θ_R); (*c*) Einstein–Johnson correction (Einstein 1942; Johnson 1942; Vanoni & Brooks 1957; Guo 2017) (Θ_E); (*d*) our universal correction (Θ). Symbols correspond to data from experiments and grain-resolved simulations (table 1). An error bar indicates the standard error and/or uncertainty range. In the absence of error bars, uncertainties are smaller than the symbol size. Except for KU17DNS ($s^{1/2}\,Ga \approx 44.86$, smooth), all data are in the rough transport regime ($s^{1/2}\,Ga > 70$). The values of h used to determine τ_b in Z22LESw and NC18EXP use a granular-physics-based bed surface definition (Pähtz & Durán 2018*b*), (2.7), and in NC18EXP∗ are based on the original definition reported by Ni & Capart (2018). For all other datasets, reported values of h are used as it has a negligible effect on the Shields numbers due to $h \gg d$. Case Z22LESn in (*d*) is based not on our sidewall correction, but on the correction that Zhang *et al.* (2025) applied to this dataset, $\Theta = 3\Theta_R$ (see text).

predominantly the consequence of the latter authors' bed surface definition (NC18EXP∗ in figure 3*d*). In fact, figure 5 shows that the bed surface elevations resulting from their definition are much below ours. It can also be seen that the vertical profiles of the non-dimensionalised local fluid shear stress Θ_{zx}^f for various flow strengths exhibit a focal point

https://doi.org/10.1017/jfm.2026.11928 Published online by Cambridge University Press

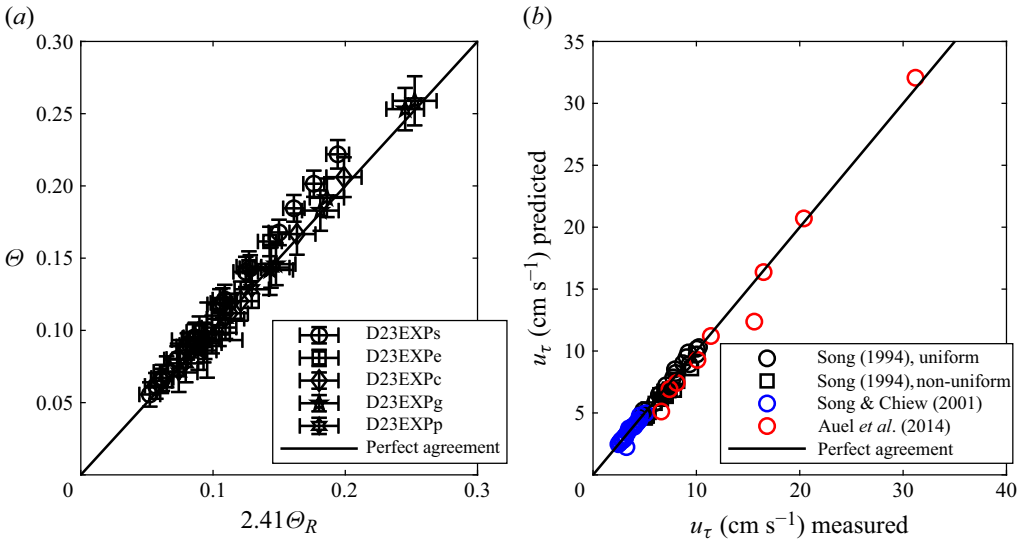


Figure 4. Channel geometry corrections. (*a*) Plot of Θ versus $2.41\Theta_R$ (using $d = c_g$ for non-spherical-grain data, as explained in § 3.1.1), based on $\tau_b = 2.41\tau_R$, the empirical correction in Deal *et al.* (2023). (*b*) Log-profile shear velocity $u_\tau \approx \sqrt{\tau_b/\rho_f}$ predicted by our sidewall correction versus measured one for experimental data from particle-free flows in open channels consisting of artificially created hydraulically rough beds ($r = d_0$ or $r = k$) and hydraulically smooth sidewalls (Song 1994; Song & Chiew 2001; Auel *et al.* 2014) (data as summarised in the tables of Guo 2015). For non-uniform flows, the bed slope $\tan\alpha$ is corrected using (1*b*) of Guo (2015).

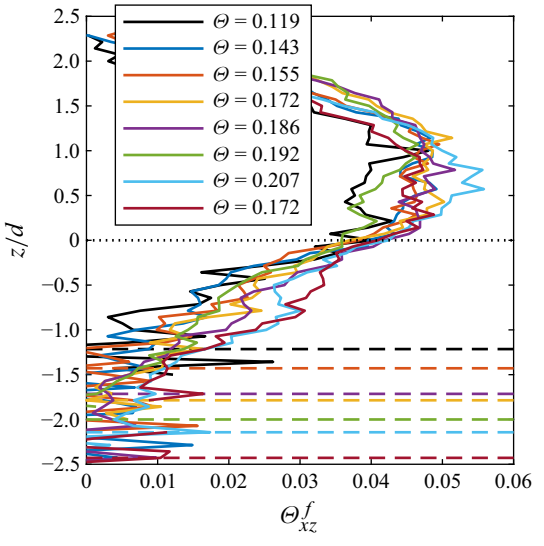


Figure 5. Independent evidence supporting our bed surface elevation definition. Vertical profiles (solid lines) of the non-dimensionalised fluid shear stress $\Theta^f_{zx} \equiv \sigma^f_{zx}/(\rho_p \tilde{g}_z d)$ for the dataset NC18EXP (Ni & Capart 2018). The data exhibit a focal point at the bed surface elevation $z = 0$ defined by (2.7): $\Theta^f_{zx}(0) \approx 0.04$, a property required for Bagnoldian-type bedload models (Pähtz & Durán 2018*b*). The fluid shear stress σ^f_{zx} is calculated from local quantities at the channel centre as described in Chauchat (2018), assuming that the mixture viscosity obeys the closure measured by Boyer *et al.* (2011) for viscous suspensions. The dashed lines correspond to the bed surface elevations determined by Ni & Capart (2018).

https://doi.org/10.1017/jfm.2026.11928 Published online by Cambridge University Press

at the bed surface elevation ($z = 0$) determined through our method (2.7), with a focal value $\Theta^f_{zx}(0) \approx 0.04$ close to the transport threshold Shields number Θ_t. As discussed in § 2.2, the occurrence of such a focal point is precisely one of the properties that we expect the bed surface to have.

3. Physical rough-bedload flux model across grain shapes, bed slopes, flow strengths and depths

In this section, we derive (§ 3.1) and validate (§ 3.3) a general bedload flux model. The validation makes use of an extended data compilation that complements the compilation for spherical grains, used in § 2 to test channel geometry correction methods, with existing data from grain-shape-controlled experiments and grain-resolved CFD-DEM simulations for non-spherical grains, and with data for spherical and non-spherical grains from grain-unresolved CFD-DEM simulations (§ 3.2).

3.1. *Model derivation*

The model is derived in two steps. First, in § 3.1.1, via generalising an existing bedload flux model (Pähtz & Durán 2020), we obtain an expression that predicts the non-dimensionalised bedload flux Q_* as a function of the excess Shields number $\Theta - \Theta_t$. Then in § 3.1.2, we explain how we calculate the unknown transport threshold Θ_t appearing in this expression.

3.1.1. *Bedload flux*

Using a numerical model coupling the RANS equations with the DEM, Pähtz & Durán (2020) simulated non-suspended sediment transport of spherical grains, and derived a general transport rate expression holding for a large range of conditions, including turbulent bedload with $s^{1/2}\,Ga \gtrsim 80$ and windblown sand:

$$Q_* = 2\kappa^{-1}\sqrt{\Theta_t}\,M_*(1 + c_M M_*), \tag{3.1}$$

with $M_* \equiv M/(\rho_p d)$. Based on the definition $M \equiv \rho_p h\langle\phi\rangle_z$ of the transport load in § 2.1, M_* can be interpreted as the number N of transported grains above a bed surface area of size $\sim d^2$. That is, M_* is a measure for the particle activity and therefore proportional to the excess Shields number $\Theta - \Theta_t$ (Ancey 2020); the proportionality factor is derived shortly. Hence for bedload transport, where $1 + c_M M_* \approx 2\sqrt{c_M M_*}$ (arithmetic mean $\approx$ geometric mean) is a good approximation as typically $c_M M_* \sim O(1)$, (3.1) predicts a bedload flux scaling similar to the classical formula by Meyer-Peter & Müller (1948).

In (3.1), $2\kappa^{-1}\sqrt{\Theta_t}$ represents the dimensionless average particle velocity at Θ_t, deduced from assuming that Θ_t corresponds to the smallest Shields number at which a quasi-continuous hopping-rebound motion (saltation) of a test grain along a stationary bed in a grain-motion-undisturbed logarithmic fluid velocity profile can be sustained, a so-called 'rebound threshold' (Pähtz *et al.* 2020). Furthermore, the term $c_M M_*$, with $c_M = 1.7$ a constant parameter determined from the simulations, encodes the rate of collisions between transported grains ($\sim M_*^2$) relative to that of grain-bed collisions ($\sim M_*^1$). In fact, (3.1) expresses the balance between global energy production due to drag (left-hand side) and energy dissipation due to grain contacts (right-hand side). In order to apply it to non-spherical grains, it is important to generalise d in a manner that retains $M_* \sim N$. Since grains transported at elevations close to the bed surface, where most transport takes place, tend to align their largest projected area A_p^{max} parallel to the bed due to torque (Jain *et al.* 2020; Zhang *et al.* 2025), implying $M \sim N\rho_p V_p / A_p^{max}$, this requirement begets

https://doi.org/10.1017/jfm.2026.11928 Published online by Cambridge University Press

$d \equiv (3/2)V_p/A_p^{max}$. From approximating grains as ellipsoids, we estimate $V_p = \pi a_g b_g c_g/6$ and $A_p^{max} = \pi a_g b_g/4$, leading to $d = c_g$ (already used in figure 4*a*).

In steady, homogeneous sediment transport, the average vertical force acting on transported grains is dominated by gravity, buoyancy and potentially fluid lift, since drag forces during the grains' upward motion tend to cancel those during their downward motion (Pähtz & Durán 2018*a*). When fluid lift is neglected, as in the simulations by Pähtz & Durán (2018*b*, 2020), this implies that the particle pressure at the bed surface $-\sigma_{zz}^p(0)$ is approximately equal to the submerged particle weight $M\tilde{g}_z$. The bed friction coefficient $\mu_b \equiv -\sigma_{zx}^p(0)/\sigma_{zz}^p(0)$ then links $M\tilde{g}_z$ to the surface particle shear stress $\sigma_{zx}^p(0)$. When further separating $\sigma_{zx}^p(0)$ into gravity and drag contributions, and assuming that particle drag on the fluid reduces the surface fluid shear stress $\sigma_{zx}^f(0)$ to a value that is just sufficient to sustain transport, one obtains (after some rearrangements) Bagnold's famous expression (Bagnold 1956; Pähtz & Durán 2018*b*)

$$M_* = \frac{\Theta - \Theta_t}{\mu_b - \tan\alpha}, \tag{3.2}$$

which is a key ingredient of numerous bedload transport and windblown sand models in the literature, including the one by Pähtz & Durán (2020). Historically, it has been assumed that μ_b is equal to μ_s, the tangent of the static angle of repose of the bulk bed material (Bagnold 1956). However, RANS-DEM simulations of turbulent bedload transport of spherical grains suggest that although constant, μ_b is actually substantially larger than μ_s ($\mu_b \approx 0.7$ versus $\mu_s \approx 0.4$) (Pähtz & Durán 2018*b*). This observation can be understood as a bed surface strengthening effect (Clark *et al.* 2017; Allen & Kudrolli 2018; Cúñez *et al.* 2022). Bedload transport increases the bed surface's ability to resist shear stress, since temporarily mobilised grains can settle again in more stable bed surface pockets (Clark *et al.* 2017). Whenever this happens, the bed surface becomes stronger relative to the bulk, i.e. $r_b \equiv \mu_b/\mu_s$ increases. This process continues until a state is reached at which the pockets that emerge at the places where grains are mobilised are equivalent to the most stable pockets that transported grains can reach (Clark *et al.* 2017). Then r_b has acquired its equilibrium value, and will no longer increase. In viscous bedload transport, where all pockets are reachable as a transported grain's kinetic energy is typically much smaller than the potential energy wells of the bed surface, $r_b \approx 3.4$ (Pähtz *et al.* 2021). However, in this study on turbulent bedload transport, where these two energy scales are of comparable size, r_b attains a smaller value as grains are too fast to probe the entire phase space of bed surface pockets (Clark *et al.* 2017). We use the value $r_b = 1.8$ suggested by the simulations by Pähtz & Durán (2018*b*), where $\mu_b \approx 0.7$ and $\mu_s \approx 0.4$, to calculate $\mu_b = r_b\mu_s$ from the measured μ_s.

In addition to using $\mu_b = r_b\mu_s$, we also generalise (3.2) to account for lift forces, defined as non-buoyancy fluid forces that act in the bed-normal direction. Neglecting particle–sidewall interactions in the particle momentum balance, a derivation analogous to that in Pähtz & Durán (2020) yields (Appendix C)

$$M_* = (\Theta - \Theta_t)/\mu^\dagger, \quad \text{with} \quad \mu^\dagger \equiv r_b\mu_s\left[\frac{1 + (s\tan\alpha/(s-1) + \chi^*)\,\overline{f_L}/\overline{f_D}}{1 + r_b\mu_s\,\overline{f_L}/\overline{f_D}}\right] - \tan\alpha, \tag{3.3}$$

where $\chi^* \equiv \chi/(\rho_p\tilde{g}_z)$, f_D is the drag force per unit mass, f_L is the lift force per unit mass divided by the fluid volume fraction $1-\phi$, and the overbar, $\bar{\cdot} \equiv \langle\phi\,\cdot\rangle_z/\langle\phi\rangle_z$, denotes the ϕ-weighted height average, i.e. the average over all transported grains. The expression for $\mu^\dagger$ takes into account that Reynolds stress gradients do not contribute to the buoyancy

https://doi.org/10.1017/jfm.2026.11928 Published online by Cambridge University Press

force (Maurin *et al.* 2018; Zhu *et al.* 2026), a recent finding that implies that there is no buoyancy force counteracting the gravitational and pressure gradient forces in the streamwise direction.

Equation (3.3) contains the single additional calibratable parameter $\overline{f_L}/\overline{f_D}$, and reduces to (3.2) if fluid lift is neglected. In real-world scenarios, one may expect $\overline{f_L}/\overline{f_D}$ to be of order unity, as suggested by measurements of drag and lift forces acting on surface roughness elements, including grains in bed surface pockets (Chepil 1958, 1961), and by DNS-DEM of sheared mobile beds (Ji *et al.* 2013). We use $\overline{f_L}/\overline{f_D} = 1.0$ because it optimises the agreement between the final model and the entire data compilation.

3.1.2. *Transport threshold*

We reiterate that the prefactor $2\sqrt{\Theta_t}/\kappa$ in (3.1) resulted from assuming that Θ_t is the smallest Shields number that permits a quasi-continuous hopping-rebound motion (saltation) of a test grain along a stationary bed in a grain-motion-undisturbed logarithmic fluid velocity profile (Pähtz & Durán 2020). In such a scenario, lift forces acting on the moving test grain are typically much smaller than drag forces due to the formers' rapid decrease with distance from the bed (Chepil 1961; Li *et al.* 2019). Then it can be shown that for conditions with $s^{1/4}\,Ga \gtrsim 200$, Θ_t in (3.1) obeys (Pähtz *et al.* 2021)

$$\Theta_t = c_t \left(r_b \mu_s - \frac{s}{s-1} \tan\alpha - \chi^* \right) / C_D, \tag{3.4}$$

where c_t is a dimensionless parameter, and C_D is an effective drag coefficient parametrising streamwise drag force acting on grains. However, in spite of the similarity of (3.4) with scaling laws classically associated with the incipient motion of a grain resting in a bed surface pocket, we emphasise again that Θ_t is not an incipient motion threshold, but a so-called rebound threshold, as defined and discussed by Pähtz *et al.* (2020, 2021). In particular, incipient motion thresholds strongly depend on turbulent fluctuations and therefore exhibit an additional dependence on h^* that is responsible for their often observed increase with bed slope $\tan\alpha$ (Lamb *et al.* 2008). By contrast, the rebound threshold Θ_t is insensitive to turbulent fluctuations (Pähtz *et al.* 2020), as was also directly shown in figure S1 of Pähtz & Durán (2018*a*) based on numerical simulation data by Maurin *et al.* (2015), and therefore always decreases with $\tan\alpha$.

The drag coefficient C_D in (3.4) is smaller than that for settling grains, $C_{DSettle} \equiv 4(s-1)gd/(3v_s^2)$ (Deal *et al.* 2023), where v_s is the terminal grain settling velocity, due to the smaller projected grain area exposed to the flow. Assuming again that transported grains tend to align their largest projected area $A_p^{max} = \pi a_g b_g/4$ parallel to the bed, the effective projected area A_p^{eff} in the streamwise direction is estimated as the geometric mean of the remaining two projected areas $\pi a_g c_g/4$ and $\pi b_g c_g/4$: $A_p^{eff} = \pi\sqrt{a_g b_g}\,c_g/4$, implying $A_p^{eff}/A_p^{max} = c_g/\sqrt{a_g b_g} \equiv S_f$, which is the Corey shape factor. Hence we obtain $C_D = S_f C_{DSettle}$ or

$$C_D = 4S_f(s-1)gd/(3v_s^2). \tag{3.5}$$

In the case of spherical grains ($S_f = 1$), typical values for the quantities in (3.4) are $\mu_s \approx 0.46$, $C_D \approx 0.43$ and $\Theta_t \approx 0.05$ (Deal *et al.* 2023), implying $c_t \approx 0.03$. We use $c_t = 0.032$ because it optimises the agreement between the final model and the entire data compilation. On the other hand, when $s^{1/4}\,Ga \lesssim 200$, viscous-sublayer effects render the scaling of Θ_t much more complicated (Pähtz *et al.* 2021). Therefore, we use (3.4) to determine Θ_t, except for the few numerical conditions with $s^{1/4}\,Ga < 200$ (BLRANSx in

https://doi.org/10.1017/jfm.2026.11928 Published online by Cambridge University Press

table 1, where 'x' stands for an arbitrary character), for which we determine Θ_t directly from the simulations, as described by Pähtz & Durán (2020). Note that the datasets J21DNS and KU17DNS in table 1, which also satisfy $s^{1/4}\,Ga < 200$, are excluded from this discussion as they violate the precondition $s^{1/2}\,Ga \gtrsim 80$ required for (3.1).

3.2. *Extended data compilation*

3.2.1. *Experiments and grain-resolved CFD-DEM simulations*

To evaluate our model, we require bedload flux datasets for shape-controlled grains, meaning that they must provide the values of v_s and S_f, required to calculate C_D in (3.5), and the value of μ_s, which affects Q_* both via the calculation of M_* in (3.3) and via the calculation of Θ_t in (3.4). The datasets by Deal *et al.* (2023), denoted as D23EXPx in table 1, and by Zhang *et al.* (2022, 2025), denoted as Z22LESx and Z25LESx in table 1, satisfy this requirement. However, we excluded from Z25LESx simulation data based on the 'artificial-shrinkage method' by Zhang *et al.* (2025), since this method has been falsified (Chen *et al.* 2026). Furthermore, in order to use the spherical-grain dataset NC18EXP by Ni & Capart (2018), who did not report μ_s, we acquired the same spheres from the same company, and measured μ_s using the funnel method (Beakawi Al-Hashemi & Baghabra Al-Amoudi 2018) in the manner described by Deal *et al.* (2023): by slowly pouring them onto an elevated disk bounded by a $2d_o$ high rim (Appendix D). Moreover, we scoured the literature and found two more usable experimental datasets for non-spherical grains: the bedload flux measurements for cylinders (R22EXPc) and lenses (R22EXPl) by Rebai *et al.* (2022). For both grain shapes, v_s (Matoušek & Zrostlík 2020) and the grain dimensions (required for S_f) have been reported, while μ_s was measured using the funnel method in a box filled with water, which was sufficiently large to rule out potential box–sidewall friction effects (private correspondence with the authors). We confirmed with DEM simulations that different procedures of conducting the funnel method have only a small effect on μ_s ($< 5\,\%$) provided that a sufficiently large number of grains is used and that there is some means of preventing grains from rolling away (such as a rim or rough bed; see Appendix D). By contrast, most other experimental datasets reported in the literature, even well-controlled ones (Lajeunesse *et al.* 2010), do not report S_f and/or μ_s.

For those datasets mentioned in the previous paragraph that were not already discussed in § 2.4.1 on the spherical-grain data compilation, we use the values of h reported in the respective studies, as justified by $h^* = h/d \gg 1$ (table 1). For more details and the calculation of the bed shear stress uncertainty, see Appendix B.

3.2.2. *Grain-unresolved CFD-DEM simulations*

Since our bedload flux model generalises (3.2), the transport load expression by Bagnold (1956), to (3.3), involving the additional parameter $\overline{f_L}/\overline{f_D} = 1.0$, we test it also for conditions to which (3.2) applies (i.e. $\overline{f_L}/\overline{f_D} = 0$). For this purpose, we add data from grain-unresolved CFD-DEM simulations to the compilation, both from existing studies (Maurin *et al.* 2018; Monthiller 2019; Pähtz & Durán 2020) and from our own new simulations, all of which were conducted using either of the numerical models described by Durán *et al.* (2012), Maurin *et al.* (2015) and Xie *et al.* (2022) (table 1; for details, see Appendix E). They differ from grain-resolved simulations in the fact that they do not resolve the flow around single grains, and they therefore incorporate empirical relations for the buoyancy, drag and lift forces acting on grains, the latter of which are typically neglected (also here, i.e. $\overline{f_L}/\overline{f_D} = 0$). They also allow us to perform thought experiments in which C_D is treated as just another control parameter, since we can artificially

https://doi.org/10.1017/jfm.2026.11928 Published online by Cambridge University Press

modify C_D through changing the drag force parameters (Appendix E); see LESCD and BLRANSCD in table 1. Another purpose for adding these data is to confront our bedload flux model with transport conditions across a much larger range of the control parameters Θ, α and h^* than that spanned by the experiments and grain-resolved simulations alone.

3.2.3. *Streamwise fluid momentum balance in BLRANSx*

The numerical model of Durán *et al.* (2012) behind the datasets BLRANSx considers a flow in an inner turbulent boundary layer of infinite height (no sidewalls). To be consistent with (2.5), we slightly modified the streamwise fluid momentum balance employed by Durán *et al.* (2012) to

$$\mathrm{d}_z \sigma_{zx}^f = \rho_f \phi g \sin\alpha + \rho_p \phi f_x^{f\to p}, \quad \text{with} \quad \sigma_{zx}^f(\infty) = \tau_b, \tag{3.6}$$

before conducting simulations, where $\rho_p \phi \boldsymbol{f}^{f\to p}$ is the fluid–particle interaction force per unit volume of the mixture. In fact, integrating (3.6) from zero to infinity, and combining the result with (C5) and $\sigma_{zx}(0) = \sigma_{zx}^f(0) + \sigma_{zx}^p(0)$, leads precisely to (2.5). Note that for the numerical model of Durán *et al.* (2012), the Shields number $\Theta \equiv \tau_b/(\rho_p \tilde{g}_z d)$ based on τ_b in (3.6) is a prescribed fixed parameter.

3.2.4. *Determination of Θ for M18RANS, M19RANSx and LESx*

Since the raw data required to determine the bed surface elevation, and thus h and τ_b, are not available for the datasets M18RANS (Maurin *et al.* 2018) and M19RANSx (Monthiller 2019) in table 1, based on the model of Maurin *et al.* (2015), we infer Θ from their reported transport-driving Shields number Θ_*, as explained in Appendix F.

3.3. *Model validation*

As a result of the wide range of control parameters and methods, especially grain-shape parameters, the data for Q_* from the grain-unresolved simulations alone (figure 6*a*), and in extension from the entire data compilation (figure 6*b*), can vary by almost an order of magnitude at a given channel-geometry-corrected Shields number Θ. Nonetheless, the predictions from our bedload flux model deviate by less than a factor 1.3 from almost all these data (figure 7). The only notable exceptions are the datasets Z25LESn and Z25LESw, which are based on the same grain shape. While the low-Θ simulations corresponding to these datasets are reproduced, their large-Θ simulations are substantially underpredicted (figures 7*a*,*d*). Among the other datasets, deviations of similar magnitude are seen only for two isolated data points: one for M19RANSt1 (figure 7*e*), and another for BLRANS1 (figure 7*f*), both of which correspond to the smallest value of Θ for each respective dataset.

As a side note, the agreement between our bedload flux model and most of the data compilation also lends support to the reliability of the grain-unresolved simulations, since if they were governed by different physics, then one would not expect them to be captured by the same physical analytical model.

4. Discussion

4.1. *The role of fluid lift in bedload transport*

Our rough-bedload flux model combines the global energy balance (3.1) after Pähtz & Durán (2020), linking the bedload flux to the transport load, with Bagnold's famous transport load expression (3.3) (Bagnold 1956), generalised to account for a non-vanishing ratio $\overline{f_L}/\overline{f_D}$ between the average lift and drag forces acting on transported grains. This is curious insofar as fluid lift is often assumed to be negligible in bulk bedload transport

https://doi.org/10.1017/jfm.2026.11928 Published online by Cambridge University Press

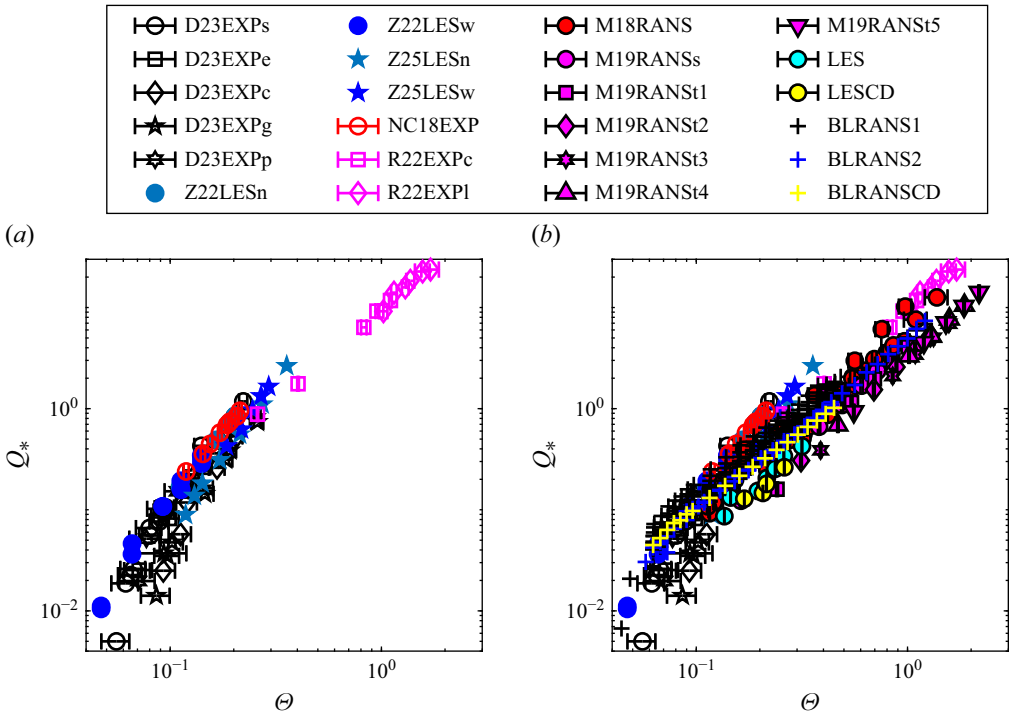


Figure 6. Data compilation exhibits substantial scatter due to grain shape and other effects. Non-dimensionalised bedload flux Q_* versus Shields number Θ, both rescaled using the generalised grain diameter definition $d \equiv (3/2)V_p/A_p^{max}$ (see text). (*a*) Symbols correspond to data from channel-geometry-corrected experiments and grain-resolved CFD-DEM simulations (table 1). (*b*) Symbols also include grain-unresolved CFD-DEM simulations (table 1). An error bar indicates the standard error and/or uncertainty range. In the absence of error bars, uncertainties are smaller than the symbol size.

(Pähtz & Durán 2020; Pähtz *et al.* 2021; Deal *et al.* 2023), mainly because once a grain is elevated above a stationary bed, the shear-induced lift force acting on it rapidly declines with elevation (Chepil 1961; Li *et al.* 2019) and may even become negative (Li *et al.* 2019; Shi & Rzehak 2019). In this regard, it is also interesting that $\overline{f_L}/\overline{f_D}$ has no bearing on the transport threshold Θ_t in (3.4). (We confirmed that including $\overline{f_L}/\overline{f_D}$ in (3.4) in a fashion after Wiberg & Smith (1987) results in failure of the overall model.) The key difference between (3.3) and (3.4) is that the former is modelling collective grain motion, whereas the latter is derived from the physical picture of a single test grain bouncing along an otherwise immobile bed. In DNS-DEM, collective grain motion is highly associated with pressure-gradient-induced lift forces of a comparable magnitude to streamwise drag forces (Ji *et al.* 2013). By contrast, in DNS of a fixed bed and a fixed particle elevated above it, such pressure-gradient-induced lift forces are much smaller than streamwise drag forces (Li *et al.* 2019). (Note that Li *et al.* (2019) called the pressure-gradient-induced lift forces 'wall-normal drag forces'.) This suggests that collective grain motion might induce pressure fluctuations and thereby substantially enhance lift forces, though more studies are needed to test this hypothesis, and if confirmed, elucidate the underlying physical mechanism.

4.2. *Test of the rough-bedload flux model of Deal et al. (2023) with independent data*

We are aware of only a single alternative bedload flux model attempting to account for grain shape: the one by Deal *et al.* (2023). These authors generalised d to the

https://doi.org/10.1017/jfm.2026.11928 Published online by Cambridge University Press

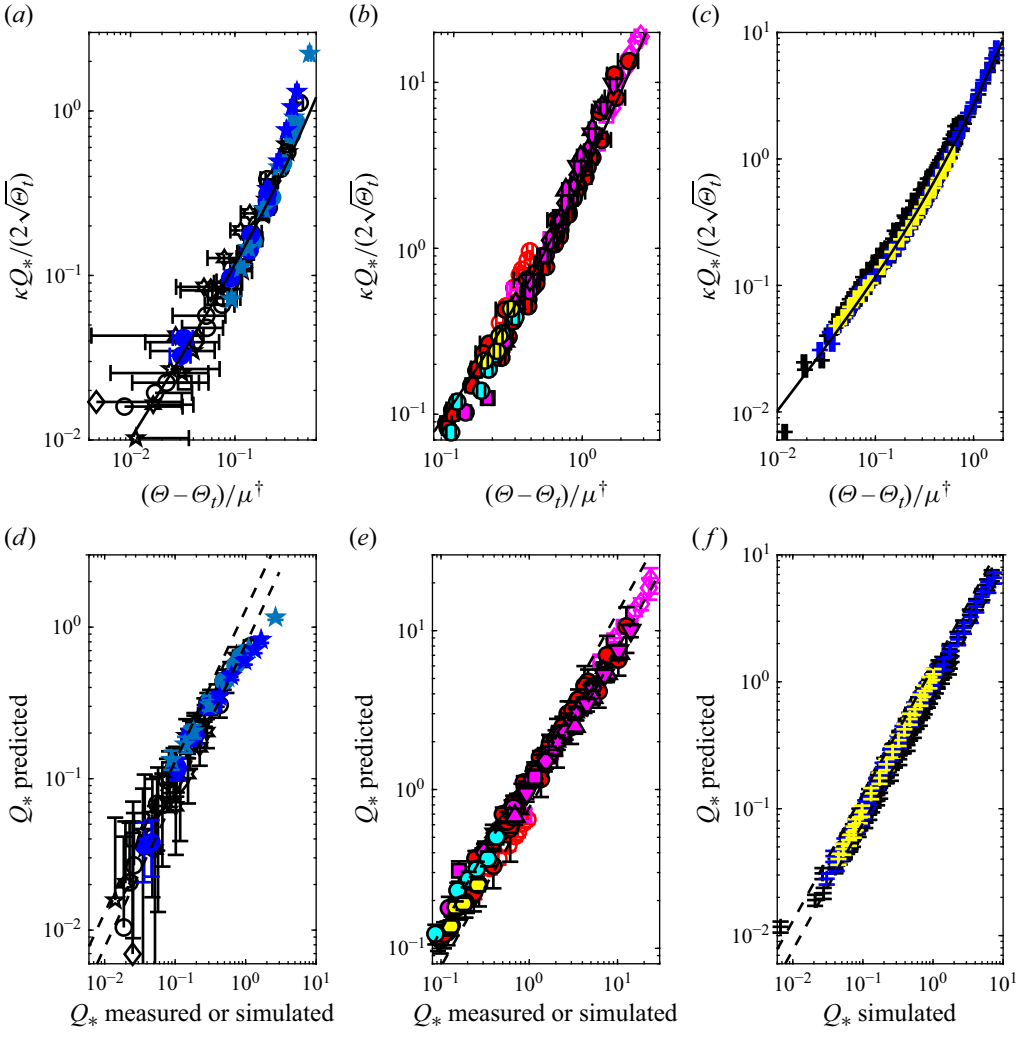


Figure 7. Test of our rough-bedload flux model across grain shapes, bed slopes, flow strengths and flow depths. (*a–c*) Normalised bedload flux $Y \equiv \kappa Q_*/(2\sqrt{\Theta_t})$ versus $X \equiv (\Theta - \Theta_t)/\mu^\dagger$ and model prediction $Y = X(1 + c_M X)$ (solid lines, from (3.1) and (3.3)). (*d–f*) Plots of Q_* predicted by (3.1) and (3.3) versus measured or simulated Q_*. Symbols correspond to channel-geometry-corrected data from a variety of methods (table 1; see figure 6 for legend). An error bar indicates the standard error and/or uncertainty range. In the absence of error bars, uncertainties are smaller than the symbol size. When $s^{1/4}\,Ga \geqslant 200$, Θ_t is calculated by (3.4). Otherwise (only BLRANSx), Θ_t is determined directly from the simulations, as described in Pähtz & Durán (2020). All grain-unresolved simulations neglect lift forces, implying $\overline{f_L}/\overline{f_D} = 0$. Almost all data in (*d–f*) fall within a factor 1.3 of the model prediction, delineated by the dashed lines.

volume-equivalent sphere diameter d_o, as opposed to the shortest grain axis $c_g \approx S_f^{2/3} d_o$ in our model, and used the modified Shields number $\Theta^{D23} \equiv \tau_b/(\rho_p \tilde{g}_z d_o)$ and modified non-dimensionalised bedload flux $Q_*^{D23} \equiv Q/(\rho_p d_o \sqrt{(s-1)g d_o})$ to quantify the flow strength and transport rate, respectively. They proposed that bedload flux data corresponding to different grain shapes collapse onto a single curve $Q_*^{D23} = f[(C^*/\mu^*)\Theta^{D23}]$, where C^* is the sphere-normalised value of $C_D d_o/c_g$ (Appendix G), and $\mu^* \equiv (\mu_s - \tan\alpha)/(\mu_o - \tan\alpha)$, with $\mu_o = \tan 24°$ the approximate value of μ_s for spheres.

https://doi.org/10.1017/jfm.2026.11928 Published online by Cambridge University Press

Deal *et al.* (2023) validated their model with their bedload flux measurements for several grain shapes, but not with other experimental data from independent sources. Here, we test their model with the independent datasets from our data compilation, sidewall-corrected with our derived universal method (figure 8). We remind the reader that when applied to the datasets by Deal *et al.* (2023), this correction yields almost the same bed shear stress τ_b as their own empirical correction (figure 4*a*), while unifying spherical-grain datasets across experimental facilities (figure 3*d*). So any unfavourable outcome of this test is likely not attributable to the application of our method. To be as fair as possible, we focus on those independent datasets obtained from experiments and grain-resolved simulations (figures 8*a–d*), and use the entire data compilation only as a secondary addition to our arguments (figures 8*e*,*f*). In addition, our main interest is not in the agreement between their model equation (solid lines in figures 8*b*,*d*) and the data, since this can be easily remedied through a change of the prefactor in that equation, but in the question of whether or not their Shields number correction reduces the scatter in the data.

It can be seen that the grain-shape correction by Deal *et al.* (2023) (figures 8*b*,*d*) much increases the scatter in the independent data when compared with the situation without correction (figures 8*a*,*c*), for both intense and weak transport conditions. In particular, the chosen range $0.05-0.25$ of the (un)corrected Shields number in figures 8(*c*) and 8(*d*) is equivalent to the range of their own experiments (Deal *et al.* 2023), and the maximum scatter in figure 8(*d*) by approximately a factor 3 occurs well within this range, at $(C^*/\mu^*)\Theta^{D23} \approx 0.14$. It is mainly caused by the dataset R22EXPc in table 1, for which $C^*/\mu^* = 0.69$, a more extreme value of C^*/μ^* than in all their experiments ($C^*/\mu^* = 0.84-1.05$) (Deal *et al.* 2023).

We believe that this poor performance chiefly results from their incorporation of C^* in their grain-shape correction of the Shields number. In fact, it was shown that models that express bedload flux as a function of the excess bed shear stress are inherently linked to the assumption by Bagnold (1956), later confirmed by Pähtz & Durán (2018*b*), that the bed friction coefficient μ_b is constant. (In the model of Deal *et al.* (2023), $\mu_b = \mu_s$, whereas $\mu_b = r_b\mu_s$ in our model.) In equilibrium, this constant friction coefficient is equal to the ratio between the average streamwise and bed-normal forces acting on transported grains, rendering the average drag force per unit mass $\overline{f_D}$ insensitive to the details of the flow. In consequence, increments of C^* (or C_D in our model) tend to be compensated by decrements of the average fluid–particle velocity difference, keeping $\overline{f_D}$ and therefore the effective transport-driving shear stress constant. Note that this reasoning is corroborated by the fact that the yellow symbols in figures 8(*e*) and 8(*f*), corresponding to conditions with artificially strongly elevated values of C^* or C_D (LESCD and BLRANSCD in table 1), shift far away from the rest of the data after employing the grain-shape correction by Deal *et al.* (2023). In contrast, they are captured by our bedload flux model (figure 7*d*) because it does not modify the Shields number Θ by a drag-dependent correction.

5. Conclusions

We have derived a universal channel geometry correction method to determine the bed shear stress that collapses spherical-grain data of the non-dimensionalised bedload flux Q_* as a function of the Shields number Θ (figure 3), obtained from experiments and grain-resolved CFD-DEM simulations, across a wide range of geometries, including narrow-deep and wide-shallow open-channel flows. It consists of a granular-physics-based method to determine the bed surface elevation and a sidewall correction derived from Kolmogorov's theory of turbulence. The latter incorporates a single parameter ($c_{bw} \approx 2.23$ in (2.10)) that is exclusively related to approximately channel-geometry-independent

https://doi.org/10.1017/jfm.2026.11928 Published online by Cambridge University Press

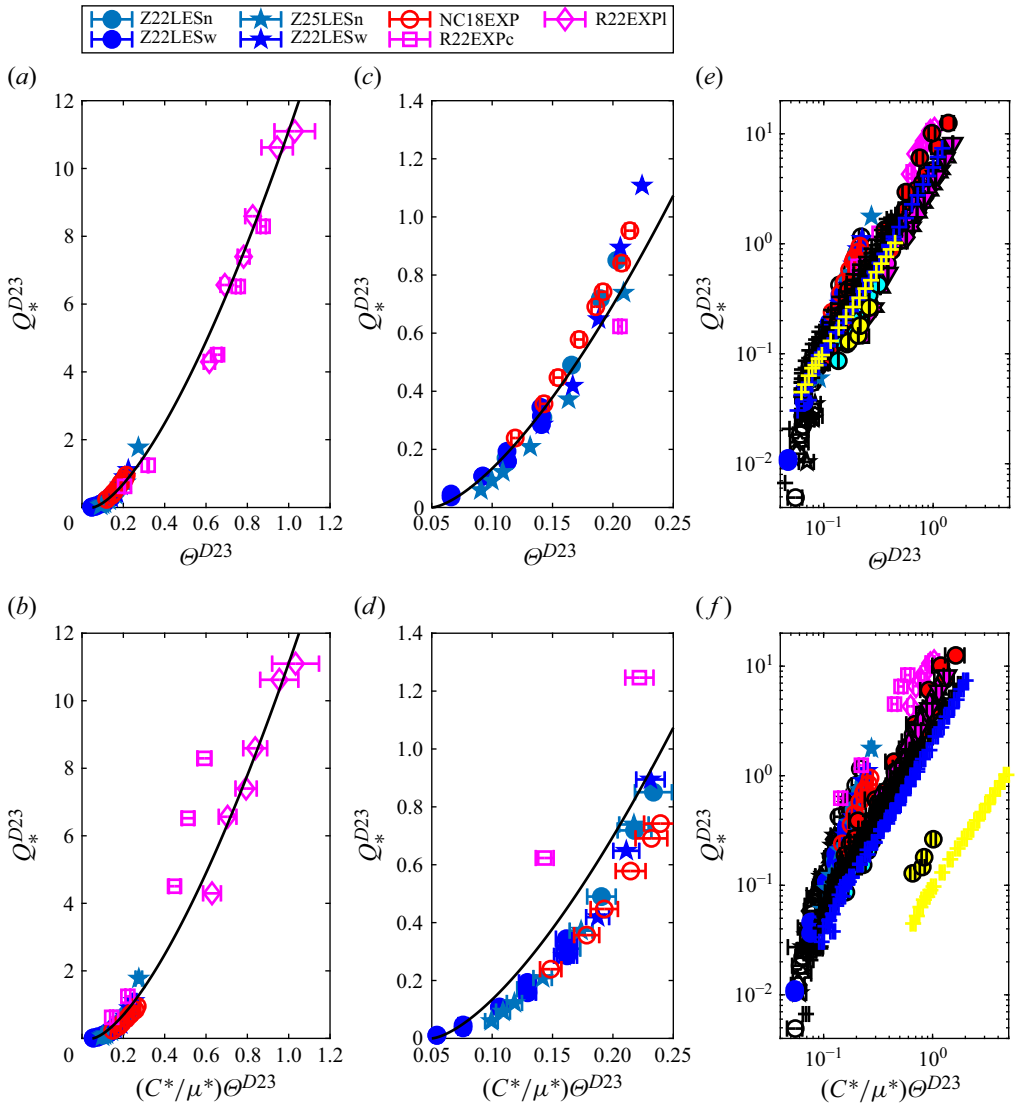


Figure 8. Test of the bedload flux model of Deal *et al.* (2023) with independent data. Plots of non-dimensionalised bedload flux Q_*^{D23} versus (*a*,*c*,*e*) shape-uncorrected Shields number Θ^{D23} and (*b*,*d*,*f*) shape-corrected Shields number $(C^*/\mu^*)\Theta^{D23}$, based on the same definitions as in Deal *et al.* (2023). Symbols in (*a–d*) correspond to data from channel-geometry-corrected experiments and grain-resolved simulations from independent studies. Symbols in (*e*,*f*) correspond to the entire channel-geometry-corrected data compilation, including D23EXPx (Deal *et al.* 2023) and data from grain-unresolved simulations (table 1; see figure 6 for legend). An error bar indicates the standard error and/or uncertainty range. In the absence of error bars, uncertainties are smaller than the symbol size. The solid lines correspond to (*a*,*c*) $Q_*^{D23} = 12(\Theta^{D23} - 0.05)^{3/2}$ and (*b*,*d*) $Q_*^{D23} = 12(\Theta^{D23}C^*/\mu^* - 0.05)^{3/2}$. The latter is the prediction by Deal *et al.* (2023).

scaling coefficients in that theory. We have applied the channel geometry correction method to a very diverse compilation of grain-shape-controlled datasets from experiments, and grain-resolved and grain-unresolved CFD-DEM simulations (table 1). An existing bedload flux model, here generalised to account for grain-shape effects, predicts almost all these data within a factor 1.3 (figure 7). By contrast, the only, to our knowledge,

https://doi.org/10.1017/jfm.2026.11928 Published online by Cambridge University Press

existing alternative bedload model accounting for grain-shape effects (Deal *et al.* 2023) clearly disagrees with the data compilation (figure 8). While our model agrees with the latter model in that the Corey shape factor S_f, static angle of repose μ_s, and settling drag coefficient $C_{DSettle}$ are the three relevant parameters for modelling grain shape, the effect of $C_{DSettle}$ on Q_* is much weaker in our model, since it appears only via the transport threshold, and not also via a modification of Θ. In § 4.2, we have reasoned that a modification of Θ via $C_{DSettle}$ is unphysical, since it conflicts with the well-established result that the friction coefficient μ_b at the interface between bed and transport layer is constant (Bagnold 1956; Pähtz & Durán 2018*b*). Another important difference between the two models is the meaning of the grain diameter d used to non-dimensionalise physical quantities. Deal *et al.* (2023) assumed that d is equal to the volume-equivalent grain diameter d_o, whereas we reasoned that d should be the size $c_g \approx S_f^{2/3} d_o$ of the shortest grain axis.

In view of the diversity of the data compilation in terms of sediment transport and channel flow conditions, and the methods on which it is based, the degree to which our relatively simple model, with only three adjustable parameters, agrees with it is remarkable (figure 7). This suggests that with the here employed sidewall correction and bed surface definition, and our physical model to predict the flux of rough bedload transport (applicable if $s^{1/2}\, Ga \gtrsim 80$, satisfied for most conditions in nature), bedload variability is largely diminished, at least for the idealised case considered here (steady flows over flat beds at short time scales). This is a prerequisite for discerning different sources of variability in the more complex situations typically encountered in nature.

Acknowledgements. The authors thank Y. Lu for helping to find grain-shape-controlled bedload transport datasets.

Funding. Z.H. acknowledges financial support from the National Key R&D Program of China (grant no. 2023YFC3008100). T.P. acknowledges financial support from the National Natural Science Foundation of China (grant nos. 12350710176, 12272344). O.D. acknowledges financial support from Texas A&M Engineering Experiment Station.

Declaration of interests. The authors report no conflict of interest.

Data availability statement. The data required to reproduce figures 3, 4(*a*), 6, 7, 8 and 11, and MATLAB code to plot them, are available online at https://doi.org/10.5281/zenodo.20921059. The measurements of μ_s resulting from the experiment in figure 9 and simulations in figure 10 are reported in table 1. The data plotted in figure 4(*b*) are from the tables of Guo (2015). The data plotted in figure 1 are from Ni & Capart (2018) and Deal *et al.* (2023), and can also be plotted using the MATLAB code. The data plotted in figures 2 and 5 are from the supplementary materials of Ni & Capart (2018). All data needed to evaluate the conclusions of the paper are present in the paper.

Author contributions. T.P. and Y.C. contributed equally.

Appendix A. The Einstein–Johnson sidewall correction

The empirical Einstein–Johnson sidewall correction calculates the friction factor ratio f_w/f_b in (2.8) as (Guo 2017)

$$\begin{gathered} f_w/f_b = R_w/R_b, \quad \text{with} \quad R_b = h(1-2R_w/b), \quad R_w = f^{-1}R\left[6\log_{10}\left[W(x)/x\right]\right]^{-2}, \\ f = 8U^{-2}gR\sin\alpha, \quad x = [9Re/(100f)]^{1/3}, \end{gathered} \tag{A1}$$

where $W(x)$ denotes the principal branch of the Lambert W function. These expressions constitute an analytical solution of the system of equations by Einstein (1942) and Johnson

https://doi.org/10.1017/jfm.2026.11928 Published online by Cambridge University Press

(1942), improving their iterative solution method as well as the graphical approximation by Vanoni & Brooks (1957).

Appendix B. Estimation of bed shear stress and its uncertainty

B.1. *Dataset NC18EXP*

For this highly resolved dataset, the profiles of $\dot{\gamma}\,\Sigma\phi$ exhibit several local maxima due to layering (figure 2). We choose the top-most local maximum at the bed surface elevation, defined in (2.7), because the profiles $\Theta^f_{zx}(z)$ exhibit a focal point there, with $\Theta^f_{zx}(0) \approx \Theta_t$ (figure 5), consistent with the theoretical expectation (Pähtz & Durán 2018*b*). It occurs $\Delta z = 31.75 \pm 0.5$ mm above the channel bottom for all flow conditions. The upper and lower bounds $\Delta z = 32.25$ mm and $\Delta z = 31.25$ mm then yield corresponding lower (h_{min}) and upper (h_{max}) bounds, respectively, of h for a given flow condition, with corresponding bed shear stress estimates $\tilde{\tau}_b(h_{max})$ and $\tilde{\tau}_b(h_{min})$, respectively, obtained from (2.8) and (2.10). Hence we estimate τ_b and its uncertainty as

$$\tau_b = \frac{1}{2}\left[\tilde{\tau}_b(h_{max}) + \tilde{\tau}_b(h_{min})\right] \pm \frac{1}{2}\left[\tilde{\tau}_b(h_{max}) - \tilde{\tau}_b(h_{min})\right]. \tag{B1}$$

B.2. *Datasets D23EXPx, R22EXPx, Z22LESx, and Z25LESx*

For these datasets, we use the reported values of h as its effect on τ_b is very small because h was much larger than the bedload layer thickness (Zhang *et al.* 2022; Zhang *et al.* 2025; Deal *et al.* 2023). Note that for the numerical datasets Z22LESx and Z25LESx, we therefore conclude that the uncertainty of τ_b is very small (smaller than the respective symbols in the plots). For the experimental datasets D23EXPx, the main source of uncertainty is the determination of the bed slope angle α. We propagate its reported uncertainty to estimate the uncertainty of τ_b. For the experimental datasets R22EXPx, the main source of uncertainty is the determination of h. We propagate its reported uncertainty to estimate the uncertainty of τ_b.

B.3. *Datasets J21DNS and KU17DNS*

As we do not have access to the raw data of these datasets, and since h was much larger than the bedload thickness (Kidanemariam & Uhlmann 2017; Jain *et al.* 2021), we use the reported values of h^* and Θ, assuming that the uncertainty of Θ is very small (smaller than the respective symbols in the plots).

B.4. *Datasets M18RANS, M19RANSx, LESx*

For these datasets, see Appendix F.

B.5. *Datasets BLRANSx*

For these datasets, $h^* = \infty$ by construction, and Θ is a prescribed parameter (no uncertainty; see § 3.2).

Appendix C. Transport load expression

To derive simple expressions for the dimensionless transport load M_*, we neglect the contributions of particle–sidewall interactions in the streamwise and vertical particle momentum balances. Then these balances read (Pähtz *et al.* 2026)

https://doi.org/10.1017/jfm.2026.11928 Published online by Cambridge University Press

$$\mathrm{d}_z\sigma_{zx}^p = -\rho_p\phi g\,\sin\alpha - \rho_p\phi f_x^{f\to p}, \tag{C1}$$

$$\mathrm{d}_z\sigma_{zz}^p = \rho_p\phi g\,\cos\alpha - \rho_p\phi f_z^{f\to p}, \tag{C2}$$

where $\rho_p\phi\boldsymbol{f}^{f\to p}$ is the fluid–particle interaction force per unit volume of the mixture. In both balance equations, we decompose $\rho_p\phi\boldsymbol{f}^{f\to p}$ into buoyancy ($\phi\mathrm{d}_z\partial_i\sigma_{ix}$) and non-buoyancy contributions, where the latter are identified as the drag plus pressure gradient ($\rho_p\phi f_D + \phi\chi$) and lift ($\rho_p\phi\tilde{f}_L$) forces per unit volume of the mixture for the streamwise and vertical directions, respectively:

$$f_x^{f\to p} = f_D + \chi/\rho_p + \mathrm{d}_z(\sigma_{zx} - \sigma_{Rezx})/\rho_p \approx f_D + \chi/\rho_p, \tag{C3}$$

$$f_z^{f\to p} = \tilde{f}_L + \mathrm{d}_z(\sigma_{zz} - \sigma_{Rezz})/\rho_p \approx \tilde{f}_L + \mathrm{d}_z\sigma_{zz}/\rho_p = \frac{\tilde{f}_L}{1-\phi} + s^{-1}g\cos\alpha. \tag{C4}$$

The buoyancy contribution in (C3) has been neglected, since the effective fluid shear stress σ_{zx} is dominated by the Reynolds stress $\sigma_{Re\,zx}$, gradients of which do not contribute to buoyancy (Maurin *et al.* 2018; Zhu *et al.* 2026). By contrast, the effective fluid pressure σ_{zz} dominates the Reynolds pressure $\sigma_{Re\,zz}$, leading to a standard buoyancy expression (e.g. Durán *et al.* 2012). Using (C3) and (C4), integration of (C1) and (C2), respectively, yields

$$\sigma_{zx}^p(0) = M\left(g\,\sin\alpha + \chi/\rho_p + \overline{f_D}\right), \tag{C5}$$

$$\sigma_{zz}^p(0) = -M\left(\tilde{g}_z - \overline{f_L}\right), \tag{C6}$$

where $f_L \equiv \tilde{f}_L/(1-\phi)$. It follows that the bed friction coefficient $\mu_b \equiv -\sigma_{zx}^p(0)/\sigma_{zz}^p(0)$ constrains the average forces acting on transported grains:

$$\mu_b = \frac{g\,\sin\alpha + \chi/\rho_p + \overline{f_D}}{\tilde{g}_z - \overline{f_L}}. \tag{C7}$$

This equation can be transformed into

$$\overline{f_D} = \frac{\mu_b\tilde{g}_z - g\,\sin\alpha - \chi/\rho_p}{1 + \mu_b\overline{f_L}/\overline{f_D}}. \tag{C8}$$

Finally, combining (C5) and (C8) with (2.5) and $\sigma_{zx} = \sigma_{zx}^f + \sigma_{zx}^p$, non-dimensionalising, and employing $\Theta - \Theta_{zx}^f(0) \equiv (\tau_b - \sigma_{zx}^f(0))/(\rho_p\tilde{g}_z d) = \Theta - \Theta_t$ (Pähtz & Durán 2018*b*), leads to (3.3).

Appendix D. Determinations of angle of repose and its uncertainty

We acquired the same spheres as those used in Ni & Capart (2018) (NC18EXP in table 1) from the same company (Chiao Dar Acry & Advertisement Co. Ltd, http://www.bridgeacry.com.tw), and measured μ_s using the funnel method (Beakawi Al-Hashemi & Baghabra Al-Amoudi 2018) in the manner described in Deal *et al.* (2023) (figure 9). Furthermore, we confirmed with DEM simulations that different measurement methods have only a small effect on μ_s provided that a sufficiently large number of grains is used and that there is some means of preventing grains from rolling away (such as a rim or a rough bed; see figure 10). Based on these simulations, we assign an uncertainty of 5 % to all μ_s measurements, including those from different studies and methods.

https://doi.org/10.1017/jfm.2026.11928 Published online by Cambridge University Press

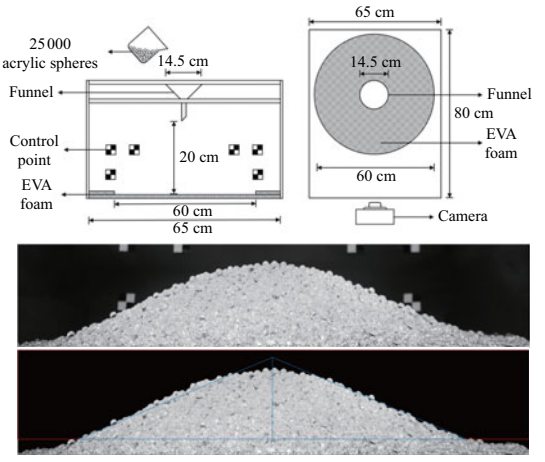


Figure 9. Measurements of μ_s for the dataset NC18EXP (table 1). We slowly poured 25 000 grains onto an elevated disk bounded by a $2d$ high rim. The angle of repose of the resulting heap is then determined as the base angle of the isosceles triangle that has the same area as the projected heap, averaged over two side-view images separated by a rotation of 90° (Elekesa & Parteli 2021).

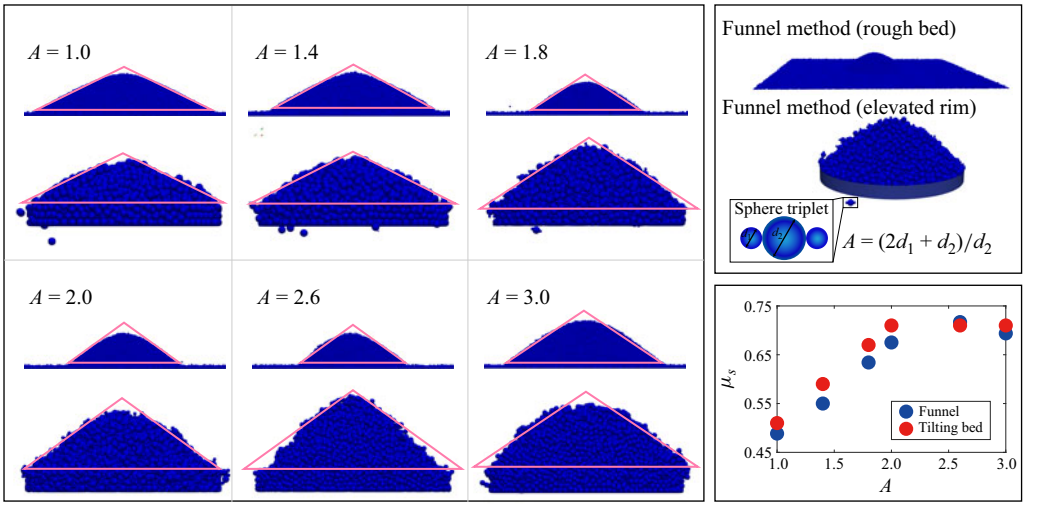


Figure 10. Numerical determination of the static angle of repose. We compare three different methods of measuring the tangent of the static angle of repose, μ_s, for the composite grains (spheres and sphere triplets) used in the grain-unresolved DEM-CFD simulations: slowly pouring a sufficient number of grains onto a rough bed consisting of spheres of the same volume-equivalent sphere diameter d_o (funnel method 1); onto an elevated disk of diameter $24d_o$ bounded by a $2d_o$ high rim (funnel method 2, exactly as described in Deal *et al.* 2023); and tilting the granular bed until the granular bulk moves (tilting method). The most reliable and reproducible results are yielded by funnel method 1, where the angle of repose is determined as the base angle of the isosceles triangle that has the same area as the projected heap, averaged over two side-view images separated by a rotation of 90° (Elekesa & Parteli 2021). For funnel method 2, the heaps exhibit too-irregular shapes when the aspect ratio A becomes too large, making a clear determination of the angle of repose difficult. However, for $A \lesssim 2$, it yields values very close to funnel method 1. The tilting method also yields similar results to funnel method 1, though it is sometimes difficult to distinguish between bulk and isolated-grain motion. We therefore decided to use funnel method 1 as the standard procedure to determine μ_s in the grain-unresolved DEM-CFD simulations.

https://doi.org/10.1017/jfm.2026.11928 Published online by Cambridge University Press

Appendix E. Grain-unresolved simulation details

E.1. *Contact parameters and μ_s in grain-unresolved CFD-DEM simulations*

The normal restitution coefficient e_n, tangential contact friction coefficient μ_c, and tangent of the static angle of repose, μ_s (determined as described in figure 10) are $(e_n, \mu_c, \mu_s) = (0.5, 0.4, 0.40)$ for the model of Maurin *et al.* (2015) and data of Maurin *et al.* (2018), $(e_n, \mu_c, \mu_s) = (0.5, 0.5, 0.49{-}0.72)$ for the model of Maurin *et al.* (2015) and data of Monthiller (2019), $(e_n, \mu_c, \mu_s) = (0.3, 0.5, 0.49)$ for the model of Xie *et al.* (2022), and $(e_n, \mu_c, \mu_s) = (0.9, 0.5, 0.38)$ for the two-dimensional model of Durán *et al.* (2012), the latter of which exhibits a lower value of μ_s because the simulation domain was quasi-two-dimensional (all grains exhibited the same fixed lateral position $y = 0$).

E.2. *Drag coefficient*

The numerical CFD-DEM models that do not resolve the sub-grain scale rely on semi-empirical relations for fluid–particle interactions. They consider buoyancy and drag forces on spheres or composite grains consisting of non-overlapping component spheres, but neglect lift forces. Following Sun *et al.* (2017), the drag force is modelled as the total force on all component spheres:

$$\boldsymbol{F}_D = \sum_i \frac{1}{8}\rho_f \pi d_i^2 \left[\left(\frac{Re_c\,\nu}{d_i \epsilon^{p_1}}\right)^{1/m} + \left(\frac{C_D^\infty\,|\boldsymbol{u}_r|}{\epsilon^{p_2}}\right)^{1/m}\right]^m \boldsymbol{u}_r, \tag{E1}$$

where d_i is the diameter of the ith component sphere, $\boldsymbol{u}_r$ is the fluid–particle velocity difference, and Re_c, C_D^∞, m, p_1 and p_2 are empirical parameters. They are $(Re_c, C_C^\infty, m, p_1, p_2) = (24.4, 0.4, 1, 3.1, 3.1)$ in Maurin *et al.* (2015), $(Re_c, C_C^\infty, m, p_1, p_2) = (24, 0.5, 2, 0, 0)$ in Durán *et al.* (2012) (nominal), $(Re_c, C_C^\infty, m, p_1, p_2) = (96, 2, 2, 0, 0)$ in Durán *et al.* (2012) (enhanced drag), $(Re_c, C_C^\infty, m, p_1, p_2) = (23.04, 0.3969, 2, p, p-1)$ in Xie *et al.* (2022) (nominal), and $(Re_c, C_C^\infty, m, p_1, p_2) = (69.12, 1.1907, 2, p, p-1)$ in Xie *et al.* (2022) (enhanced drag), with $p = 3.7 - 0.65\exp[-(1.5 - \log_{10}(\epsilon\,|\boldsymbol{u}_r|\,d_i/\nu))^2/2]$. Dividing (E1) by the grain weight $(\pi/6)\sum_i d_i^3$ leads to an expression for the ratio between the drag acceleration $\boldsymbol{a}_D$ and submerged gravitational acceleration $\tilde{g} \equiv (1 - 1/s)g$ in terms of non-dimensionalised quantities:

$$\frac{\boldsymbol{a}_D}{\tilde{g}} = \frac{3}{4}\left[\left(\frac{Re_c}{\widetilde{Ga}\,\epsilon^{p_1}}\right)^{1/m} + \left(\frac{C_D^\infty\,|\tilde{\boldsymbol{u}}_r|}{\epsilon^{p_2}}\right)^{1/m}\right]^m \tilde{\boldsymbol{u}}_r, \tag{E2}$$

where $\tilde{\boldsymbol{u}}_r \equiv \boldsymbol{u}_r/\sqrt{s\tilde{g}d}$, with $d \equiv (3/2)V_p/A_p^{max} = \sum_i d_i^3 / \sum_i d_i^2$, is the non-dimensionalised fluid–particle velocity difference, and

$$\widetilde{Ga} \equiv \frac{\sqrt{\left(\sum_i d_i^2\right)\left(\sum_i d_i^3\right)}}{\sum_i d_i}\sqrt{s\tilde{g}}/\nu, \tag{E3}$$

a quantity similar to the Galileo number. From (E2), one obtains the non-dimensionalised settling velocity $\tilde{v}_s$ of a single composite grain in quiescent fluid ($\epsilon = 1$) as (Pähtz *et al.* 2021)

$$\tilde{v}_s = \left[\sqrt{\frac{1}{4}\sqrt[m]{\left(\frac{Re_c}{C_D^\infty\,\widetilde{Ga}}\right)^2} + \sqrt[m]{\frac{4}{3C_D^\infty}}} - \frac{1}{2}\sqrt[m]{\frac{Re_c}{C_D^\infty\,\widetilde{Ga}}}\right]^m, \tag{E4}$$

https://doi.org/10.1017/jfm.2026.11928 Published online by Cambridge University Press

and subsequently the drag coefficient as

$$C_D = \frac{4(s-1)gd}{3v_s^2} = \frac{4}{3\tilde{v}_s^2}. \tag{E5}$$

Here, we used that a composite grain is treated as if the projected area of all its component spheres is always, regardless of its orientation relative to the flow, fully exposed to the flow, which follows from (E1). That is, the total projected area seen by the flow, $A_p = (\pi/4)\sum_i d_i^2$, is constant, and therefore $A_p^{eff} = A_p^{max}$ and $C_D = C_{DSettle}$.

Appendix F. Determination of Θ for M18RANS, M19RANSx and LESx

For the datasets M18RANS (Maurin *et al.* 2018) and M19RANSx (Monthiller 2019) in table 1, based on the model of Maurin *et al.* (2015), only the transport-driving Shields number Θ_* is reported. Maurin *et al.* (2015) defined $\Theta_* \equiv \tau_{cl}/(\rho_p \tilde{g}_z d)$ as the Shields number based on the clear-water fluid shear stress τ_{cl} on the top of the bedload layer:

$$\tau_{cl} \equiv \max \sigma_{zx}^f(z). \tag{F1}$$

Using $\tau_b \propto h$ for their sidewall-free channels, τ_{cl} therefore defines an effective clear-flow depth as

$$h_{cl} \equiv h\tau_{cl}/\tau_b, \tag{F2}$$

and subsequently an effective bedload layer thickness above the bed surface as

$$h_p \equiv h - h_{cl}. \tag{F3}$$

The latter is linked to the transport load M via

$$M = \rho_p h_p \underline{\phi}, \tag{F4}$$

with $\underline{\phi} \equiv (1/h_p)\int_0^h \phi \mathrm{d}z \approx (1/h_p)\int_0^{h_p} \phi\, \mathrm{d}z$ the approximate average of the particle volume fraction ϕ over the bedload layer thickness. Combining the above relations and non-dimensionalising the result yields

$$\Theta = \Theta_* \left(1 + \frac{M_*}{\underline{\phi} h_{cl}^*}\right), \tag{F5}$$

where $h_{cl}^* \equiv h_{cl}/d$ is the dimensionless clear-flow depth.

To determine the parameter $\underline{\phi}$ in (F5), we combine (F5) with (3.2), valid for the grain-unresolved simulations due to $\overline{f_L}/\overline{f_D} = 0$, yielding

$$\underline{\phi} = J\left(1 - \frac{\Theta_* - \Theta_t}{(r_b\mu_s - \tan\alpha)M_*}\right)^{-1}, \tag{F6}$$

with $J \equiv \Theta_*/[h_{cl}^*(r_b\mu_s - \tan\alpha)]$. The unknown values of M_* in (F6) can be estimated from the simulation data of Q_* via (3.1), using the predicted values of Θ_t from (3.4). Figure 11 shows the resulting estimates of $\underline{\phi}$ as a function of J for the grain-unresolved datasets M18RANS, M19RANSx, LES and LESCD. Note that the estimates for $J \lesssim 0.05$ cannot be trusted, since they are very sensitive to even slight variations in the simulation data of Θ_*, h_{cl}^*, and especially Q_*, explaining the large scatter and the occasionally unphysically large values of $\underline{\phi}$ for low J. However, this is not a serious issue, since for weak transport conditions, Θ_* is close to Θ no matter the precise value of $\underline{\phi}$ as M_* in (F5) becomes small. By contrast, for $J \gtrsim 0.05$, the estimations of $\underline{\phi}$ from the simulation data

https://doi.org/10.1017/jfm.2026.11928 Published online by Cambridge University Press

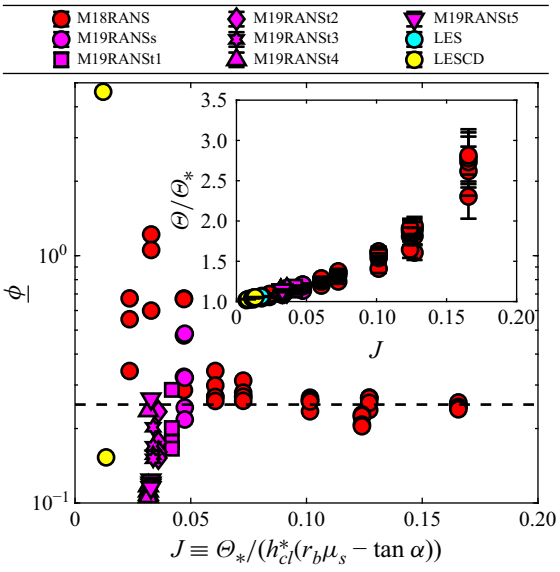


Figure 11. Determination of transport-layer-averaged particle volume fraction $\underline{\phi}$, estimated from the Q_* data as described in the text, versus J. Symbols correspond to grain-unresolved CFD-DEM simulations (table 1). The dashed line indicates the value $\underline{\phi} = 0.25$ exhibited for large J, where the ratio Θ/Θ_* deviates from unity the most. Inset: estimate of Θ/Θ_* resulting from $\underline{\phi} = 0.25$, where the error bars correspond to the propagated uncertainty of μ_s, required for predicting M_* and therefore Θ, as described in the text.

scatter relatively little between only approximately 0.2 and 0.3 (figure 11). In particular, for the most intense conditions, $\underline{\phi} \approx 0.25$, which is a reasonable value as it is approximately half of $\phi(0)$ for intense transport conditions (Pähtz & Durán 2018*b*). We therefore fix $\underline{\phi} = 0.25$ in (F5) as a simple means to relate Θ to Θ_* for arbitrary conditions through (F5). The ratio Θ/Θ_* resulting from this choice is shown in the inset of figure 11.

Although we have used the M_* values estimated from the Q_* data via (3.1) to obtain $\underline{\phi} = 0.25$, we do not do so when estimating Θ from (F5), in order to avoid an implicit dependence of Θ on Q_*. Instead, we obtain Θ from the values of M_* predicted by (3.3). The uncertainty of Θ then corresponds to the propagated uncertainty of μ_s in the calculation of Θ via (3.3) and (F5).

Appendix G. Sphere-normalised drag coefficient after Deal *et al.* (2023)

Deal *et al.* (2023) defined the sphere-normalised drag coefficient C^* as

$$C^* \equiv S_f v_o^2/v_s^2, \tag{G1}$$

where v_o is the theoretical value of the settling velocity of spheres, given via (Dietrich 1982; Deal *et al.* 2023)

$$v_{o*} = -3.81564 + 1.94593D_* - 0.09016D_*^2 - 0.00855D_*^3 + 0.00075D_*^4, \tag{G2}$$

with $v_{o*} \equiv \log_{10} v_o^3/[(s-1)g\nu]$ and $D_* \equiv \log_{10}(s-1)gd_o^3/\nu^2$. Since these expressions are based on the volume-equivalent sphere diameter d_o, as opposed to the shortest grain axis c_g in our model, C^* is linked to the drag coefficient C_D in (3.5) through $C^* = C_D d_o/(C_o c_g)$, where $C_o \equiv 4(s-1)gd_o/(3v_o^2)$.

https://doi.org/10.1017/jfm.2026.11928 Published online by Cambridge University Press

References

Agudo, J.R., Illigmann, C., Luzi, G., Laukart, A., Delgado, A. & Wierschem, A. 2017 Shear-induced incipient motion of a single sphere on uniform substrates at low particle Reynolds numbers. *J. Fluid Mech.* **825**, 284–314.

Allen, B. & Kudrolli, A. 2018 Granular bed consolidation, creep, and armoring under subcritical fluid flow. *Phys. Rev. Fluids* **3** (7), 074305.

Ancey, C. 2020 Bedload transport: a walk between randomness and determinism. Part 1. The state of the art. *J. Hydraul. Res.* **58** (1), 1–17.

Ancey, C. & Recking, A. 2023 Scaling behavior of bedload transport: what if Bagnold was right? *Earth-Sci. Rev.* **246**, 104571.

Antonia, R.A. & Pearson, B.R. 2000 Reynolds number dependence of velocity structure functions in a turbulent pipe flow. *Flow Turbul. Combust.* **64** (2), 95–117.

Armanini, A. & Cavedon, V. 2019 Bed-load through emergent vegetation. *Adv. Water Resour.* **129**, 250–259.

Auel, C., Albayrak, I. & Boes, R.M. 2014 Turbulence characteristics in supercritical open channel flows: effects of Froude number and aspect ratio. *J. Hydraul. Engng* **140** (4), 04014004.

Aussillous, P., Chauchat, J., Pailha, M., Médale, M. & Guazzelli, É. 2013 Investigation of the mobile granular layer in bedload transport by laminar shearing flows. *J. Fluid Mech.* **736**, 594–615.

Bagnold, R.A. 1956 The flow of cohesionless grains in fluid. *Phil. Trans. R. Soc. Lond. A* **249** (964), 235–297.

Baker, V.R., Hamilton, C.W., Burr, D.M., Gulick, V.C., Komatsu, G., Luo, W., Rice, J.W. & Rodriguez, J.A.P. 2015 Fluvial geomorphology on Earth-like planetary surfaces: a review. *Geomorphology* **245**, 149–182.

Beakawi Al-Hashemi, H.M. & Baghabra Al-Amoudi, O.S. 2018 A review on the angle of repose of granular materials. *Powder Technol.* **330**, 397–417.

Boyer, F., Guazzelli, É. & Pouliquen, O. 2011 Unifying suspension and granular rheology. *Phys. Rev. Lett.* **107** (18), 188301.

Capart, H. & Fraccarollo, L. 2011 Transport layer structure in intense bed-load. *Geophys. Res. Lett.* **38** (20), L20402.

Carrillo, V., Petrie, J., Timbe, L., Pacheco, E., Astudillo, W., Padilla, C. & Cisneros, F. 2022 Validation of an experimental procedure to determine bedload transport rates in steep channels with coarse sediment. *Water* **13**, 672.

Charru, F., Andreotti, B. & Claudin, P. 2013 Sand ripples and dunes. *Annu. Rev. Fluid Mech.* **45**, 469–493.

Charru, F., Mouilleron, H. & Eiff, O. 2004 Erosion and deposition of particles on a bed sheared by a viscous flow. *J. Fluid Mech.* **519**, 55–80.

Chauchat, J. 2018 A comprehensive two-phase flow model for unidirectional sheet-flows. *J. Hydraul. Res.* **56** (1), 15–28.

Chen, Y., Durán, O. & Pähtz, T. 2026 On the testing of grain shape corrections to bedload transport equations with grain-resolved numerical simulations. *Earth Surf. Dyn.* **14**, 75–83.

Chepil, W.S. 1958 The use of evenly spaced hemispheres to evaluate aerodynamic forces on a soil surface. *Trans. Am. Geophys. Union* **39**, 397–403.

Chepil, W.S. 1961 The use of spheres to measure lift and drag on wind-eroded soil grains. *Soil Sci. Soc. Am. J.* **25** (5), 343–345.

Clark, A.H., Shattuck, M.D., Ouellette, N.T. & O'Hern, C.S. 2017 Role of grain dynamics in determining the onset of sediment transport. *Phys. Rev. Fluids* **2** (3), 034305.

Cúñez, F.D., Franklin, E.M., Houssais, M., Arratia, P. & Jerolmack, D.J. 2022 Strain hardening by sediment transport. *Phys. Rev. Res.* **4** (2), L022055.

Deal, E., Venditti, J.G., Benavides, S.J., Bradley, R., Zhang, Q., Kamrin, K. & Perron, J.T. 2023 Grain shape effects in bed load sediment transport. *Nature* **613**, 298–302.

Dhont, B. & Ancey, C. 2018 Are bedload transport pulses in gravel bed rivers created by bar migration or sediment waves? *Geophys. Res. Lett.* **45** (11), 5501–5508.

Dietrich, W.E. 1982 Settling velocity of natural particles. *Water Resour. Res.* **18** (6), 1615–1626.

Durán, O., Andreotti, B. & Claudin, P. 2012 Numerical simulation of turbulent sediment transport, from bed load to saltation. *Phys. Fluids* **24** (10), 103306.

Durán Vinent, O., Andreotti, B., Claudin, P. & Winter, C. 2019 A unified model of ripples and dunes in water and planetary environments. *Nat. Geosci.* **12**, 345–350.

Einstein, H.A. 1942 Formulas for the transportation of bedload. *Trans. ASCE* **107**, 561–597.

https://doi.org/10.1017/jfm.2026.11928 Published online by Cambridge University Press

ELEKESA, F. & PARTELI, E.J.R. 2021 An expression for the angle of repose of dry cohesive granular materials on Earth and in planetary environments. *Proc. Natl Acad. Sci. USA* **118** (38), e2107965118.
FREY, P. 2014 Particle velocity and concentration profiles in bedload experiments on a steep slope. *Earth Surf. Process. Landf.* **39** (5), 646–655.
FREY, P., DUFRESNE, M., BÖHM, T., JODEAU, M. & ANCEY, C. 2006 Experimental study of bed load on steep slopes. In *River Flow* (ed. Ferreira, Alves, Leal & Cardoso), pp. 887–893. Taylor & Francis.
GIOIA, G. & BOMBARDELLI, F.A. 2002 Scaling and similarity in rough channel flows. *Phys. Rev. Lett.* **88** (1), 014501.
GIOIA, G. & CHAKRABORTY, P. 2006 Turbulent friction in rough pipes and the energy spectrum of the phenomenological theory. *Phys. Rev. Lett.* **96** (4), 044502.
GUO, J. 2015 Sidewall and non-uniformity corrections for flume experiments. *J. Hydraul. Res.* **53** (2), 218–229.
GUO, J. 2017 Exact procedure for Einstein–Johnson's sidewall correction in open channel flow. *J. Hydraul. Engng* **143** (4), 06016027.
HOUSSAIS, M., ORTIZ, C.P., DURIAN, D.J. & JEROLMACK, D.J. 2015 Onset of sediment transport is a continuous transition driven by fluid shear and granular creep. *Nat. Commun.* **6**, 6527.
JAIN, R., TSCHISGALE, S. & FRÖHLICH, J. 2020 Effect of particle shape on bedload sediment transport in case of small particle loading. *Meccanica* **55**, 299–315.
JAIN, R., TSCHISGALE, S. & FRÖHLICH, J. 2021 Impact of shape: DNS of sediment transport with non-spherical particles. *J. Fluid Mech.* **916**, A38.
JI, C., MUNJIZA, A., AVITAL, E., MA, J. & WILLIAMS, J.J.R. 2013 Direct numerical simulation of sediment entrainment in turbulent channel flow. *Phys. Fluids* **25** (5), 056601.
JOHNSON, J.W. 1942 The importance of considering sidewall friction in bed-load investigations. *Civil Engng* **12**, 329–332.
KIDANEMARIAM, A.G. 2016 The formation of patterns in subaqueous sediment. PhD thesis, Karlsruhe Institute of Technology.
KIDANEMARIAM, A.G. & UHLMANN, M. 2017 Formation of sediment patterns in channel flow: minimal unstable systems and their temporal evolution. *J. Fluid Mech.* **818**, 716–743.
LAJEUNESSE, E., MALVERTI, L. & CHARRU, F. 2010 Bed load transport in turbulent flow at the grain scale: experiments and modeling. *J. Geophys. Res.: Earth Surf.* **115** (F4), F04001.
LAMB, M.P., DIETRICH, W.E. & VENDITTI, J.G. 2008 Is the critical Shields stress for incipient sediment motion dependent on channel-bed slope? *J. Geophys. Res.* **113**, F02008.
LI, X., BALACHANDAR, S., LEE, H. & BAI, B. 2019 Fully resolved simulations of a stationary finite-sized particle in wall turbulence over a rough bed. *Phys. Rev. Fluids* **4** (9), 094302.
MATOUŠEK, V. & ZROSTLÍK, Š. 2020 Collisional transport model for intense bed load. *J. Hydrol. Hydromech.* **68** (1), 60–69.
MAURIN, R., CHAUCHAT, J., CHAREYRE, B. & FREY, P. 2015 A minimal coupled fluid–discrete element model for bedload transport. *Phys. Fluids* **27** (11), 113302.
MAURIN, R., CHAUCHAT, J. & FREY, P. 2018 Revisiting slope influence in turbulent bedload transport: consequences for vertical flow structure and transport rate scaling. *J. Fluid Mech.* **839**, 135–156.
MEYER-PETER, E. & MÜLLER, R. 1948 Formulas for bed-load transport. In *Proceedings of the International Association for Hydraulic Research, 3rd Annual Meeting, Stockholm, Sweden*, pp. 39–64. International Association for Hydraulic Research (IAHR).
MONTHILLER, R. 2019 Particle shape influence on turbulent bedload transport. Master's thesis, ENSEEIHT, University of Toulouse.
NI, W.J. & CAPART, H. 2018 Stresses and drag in turbulent bed load from refractive index-matched experiments. *Geophys. Res. Lett.* **45**, 7000–7009.
NIKITIN, N.V., NICOUD, F., WASISTHO, B., SQUIRES, K.D. & SPALART, P.R. 2000 An approach to wall modeling in large-eddy simulations. *Phys. Fluids* **12** (7), 1629.
NIKURADSE, J. 1933 Strömungsgesetze in rauhen Röhren. *VDI-Forschungsheft* **361**, 1–22. English translation: 'Laws of flow in rough pipes' (NACA TM 1292, 1950).
OURIEMI, M., AUSSILLOUS, P., MEDALE, M., PEYSSON, Y. & GUAZZELLI, É. 2007 Determination of the critical Shields number for particle erosion in laminar flow. *Phys. Fluids* **19** (6), 061706.
PÄHTZ, T., CHEN, Y., ZHU, R., THOLEN, K. & HE, Z. 2026 Coarse-graining particulate two-phase flow. *Granul. Matt.* **28**, 20.
PÄHTZ, T., CLARK, A.H., VALYRAKIS, M. & DURÁN, O. 2020 The physics of sediment transport initiation, cessation, and entrainment across aeolian and fluvial environments. *Rev. Geophys.* **58** (1), e2019RG000679.
PÄHTZ, T. & DURÁN, O. 2018*a* The cessation threshold of nonsuspended sediment transport across aeolian and fluvial environments. *J. Geophys. Res.: Earth Surf.* **123** (8), 1638–1666.

https://doi.org/10.1017/jfm.2026.11928 Published online by Cambridge University Press

PÄHTZ, T. & DURÁN, O. 2018*b* Universal friction law at granular solid–gas transition explains scaling of sediment transport load with excess fluid shear stress. *Phys. Rev. Fluids* **3** (10), 104302.
PÄHTZ, T. & DURÁN, O. 2020 Unification of aeolian and fluvial sediment transport rate from granular physics. *Phys. Rev. Lett.* **124** (16), 168001.
PÄHTZ, T., LIU, Y., XIA, Y., HU, P., HE, Z. & THOLEN, K. 2021 Unified model of sediment transport threshold and rate across weak and intense subaqueous bedload, windblown sand, and windblown snow. *J. Geophys. Res.: Earth Surf.* **126** (4), e2020JF005859.
POGGIALI, V., MASTROGIUSEPPE, M., HAYES, A.G., SEU, R., BIRCH, S.P.D., LORENZ, R., GRIMA, C. & HOFGARTNER, J.D. 2016 Liquid-filled canyons on Titan. *Geophys. Res. Lett.* **43** (15), 7887–7894.
REBAI, D., BERZI, D., BALLIO, F. & MATOUSEK, V. 2022 Experimental comparison of inclined flows with and without intense sediment transport: flow resistance and surface elevation. *J. Hydraul. Engng* **148** (12), 04022026.
RECKING, A. 2010 A comparison between flume and field bed load transport data and consequences for surface-based bed load transport prediction. *Water Resour. Res.* **46** (3), W03518.
SCHIEBER, J. 2016 Mud re-distribution in epicontinental basins – exploring likely processes. *Mar. Petrol. Geol.* **71**, 119–133.
SHCHEPETKINA, A., GINGRAS, M.K., MÁNGANO, M.G. & BUATOIS, L.A. 2019 Fluvio-tidal transition zone: terminology, sedimentological and ichnological characteristics, and significance. *Earth-Sci. Rev.* **192**, 214–235.
SHI, P. & RZEHAK, R. 2019 Lift forces on solid spherical particles in unbounded flows. *Chem. Engng Sci.* **208**, 115145.
SONG, T. 1994 Velocity and turbulence distribution in nonuniform and unsteady open-channel flow. PhD thesis, Swiss Federal Institute of Technology EPFL.
SONG, T. & CHIEW, Y.M. 2001 Turbulence measurement in non-uniform open-channel flow using acoustic Doppler velocimeter (ADV). *J. Engng Mech.* **127** (3), 219–232.
SUN, R., XIAO, H. & SUN, H. 2017 Realistic representation of grain shapes in CFD-DEM simulations of sediment transport with a bonded-sphere approach. *Adv. Water Resour.* **107**, 421–438.
TENNEKES, H. & LUMLEY, J.L. 1972 *A First Course in Turbulence*. MIT Press.
VANONI, V.A. & BROOKS, N.H. 1957 *Laboratory Studies of the Roughness and Suspended Load of Alluvial Streams*. California Institute of Technology. Report E-68.
WIBERG, P.L. & SMITH, J.D. 1987 Calculations of the critical shear stress for motion of uniform and heterogeneous sediments. *Water Resour. Res.* **23** (8), 1471–1480.
XIE, J., HU, P., PÄHTZ, T., HE, Z. & CHENG, N. 2022 Fluid–particle interaction regimes during the evolution of turbidity currents from a coupled LES/DEM model. *Adv. Water Resour.* **163**, 104171.
YAGER, E.M., VENDITTI, J.G., SMITH, H.J. & SCHMEECKLE, M.W. 2018 The trouble with shear stress. *Geomorphology* **323**, 41–50.
YANG, S.Q., LIM, S.Y. & MCCORQUODALE, J.A. 2005 Investigation of near wall velocity in 3-D smooth channel flows. *J. Hydraul. Res.* **43** (2), 149–157.
YANG, X.I.A., PARK, G.I. & MOIN, P. 2017 Log-layer mismatch and modeling of the fluctuating wall stress in wall-modeled large-eddy simulations. *Phys. Rev. Fluids* **2** (10), 104601.
ZHANG, Q., DEAL, E., PERRON, J.T., VENDITTI, J.G., BENAVIDES, S.J., RUSHLOW, M. & KAMRIN, K. 2022 Fluid-driven transport of round sediment particles: from discrete simulations to continuum modeling. *J. Geophys. Res.: Earth Surf.* **127** (7), e2021JF006504.
ZHANG, Q., DEAL, E., PERRON, J.T., VENDITTI, J.G., BENAVIDES, S.J., RUSHLOW, M. & KAMRIN, K. 2025 Discrete simulations of fluid-driven transport of naturally shaped sediment particles. *J. Geophys. Res.: Earth Surf.* **130** (5), e2024JF007937.
ZHU, R., CHEN, Y., THOLEN, K., HE, Z. & PÄHTZ, T. 2026 On buoyancy in disperse two-phase flow and its impact on well-posedness of two-fluid models. https://doi.org/10.48550/arXiv.2507.21602.

https://doi.org/10.1017/jfm.2026.11928 Published online by Cambridge University Press